MODELING THE PHOTO-OXIDATIVE DEGRADATION MECHANISMS OF THIOPHENE IN BORON-CONTAINING OLIGOTHIOPHENES AND THE IGNITION REACTIONS OF HYPERGOLIC PROPELLANTS

by

Oğuzhan Kucur

B.S., Chemistry, Bogazici University, 2017

Submitted to the Institute for Graduate Studies in
Science and Engineering in partial fulfillment of
the requirements for the degree of
Master and Science

Graduate Program in Chemistry

Boğaziçi University

2019

ACKNOWLEDGEMENTS

First of all, I am eager express my gratitude to my advisor, Prof. Viktorya Aviyente for giving me an opportunity to work with her during the final year of bachelor's studies and providing me with extensive guidance, immense patience and academic motivation throughout my graduate years as well as my journey in the subfield of computational chemistry. Owing to her, I have grown fond of theoretical chemistry and found the inspiration to carry out my master's thesis projects. I also want to thank my thesis supervisor Şaron Çatak for broadening my knowledge and encouraging me to further extents.

I wish to thank the rest of my examining committee, Prof. Antonio Monari, Prof. Neren Ökte. Besides that, I am thankful to Prof. Antonio Monari from University of Lorraine also for accepting me as a summer intern and letting me be a part Laboratoire de Physique et Chimie Théoriques. Gaining his valuable insights enlarged my vision.

Furthermore, I wish to indicate my appreciation to Prof. İlknur Doğan for her kindness and instruction throughout the courses I have taken from her in my graduate and undergraduate studies. Her teaching has rendered organic chemistry more understandable for me.

I feel fortunate to be a part of CCBG family between 2016-2019. Members of CCBG made it possible to work coperatively in a harmonious environment. I am grateful to them for their support in this process of taking courses and exploring computational chemistry.

I would like to end this by thanking my family. My mother has brought me up with a hunger for knowledge, always feeding my curiosity with attention. Evidently, I would not be writing the thesis without her constant love and support throughout my life.

ABSTRACT

MODELING THE PHOTO-OXIDATIVE DEGRADATION MECHANISMS OF THIOPHENE IN BORON-CONTAINING OLIGOTHIOPHENES AND THE IGNITION REACTIONS OF HYPERGOLIC PROPELLANTS

This dissertation, employs computational methods to investigate i) the photo-oxidative degradation mechanisms of thiophene in boron-containing oligothiophenes and ii) the ignition reactions of hypergolic propellants.

In the first part of this study, reactions betweeen thiophene group of boron-containing oligothiophenes and reactive oxygen species are analyzed. Reactive oxygen species used in this work can be listed as hydroxyl radical, hydroperoxyl radical, singlet molecular oxygen ($^1O_2$) and triplet molecular oxygen ($^3O_2$). Transition state structure for each reaction has been located. Free energy profile for every reaction mechanism is analyzed.

In the second part of this study, the ignition reactions of hypergolic propellants are assessed. The reactions between the fuels and nitric acid are modeled. The initial salt formation is very exothermic and it supplies the energy for the ignition reactions: H-abstraction, β-scission and N-N_2 bond fission reactions. Reactants and products of the salt formation reactions are investigated by using the solvation model implicitly at 298.15°C in nitric acid. The transition state structures of the remaining reactions are located in vacuum at 423K. Analysis of their reaction kinetics has shed light to the ignition delay time difference between different fuels.

ÖZET

BORON İÇEREN OLİGOTİYOFENLERDEKİ TİYOFENİN FOTO-OKSİDATİF BOZUNMA MEKANİZMALARININ VE HİPERGOLİK YAKITLARIN YANMA TEPKİMELERİNİN MODELLENMESİ

Bu tez, hesapsal yöntemler kullanarak i) boron içeren oligotiyofenlerdeki tiyofenin foto-oksidatif bozunma mekanizmalarını ve ii) hipergolik yakıtların yanma tepkimelerini incelemektedir.

Çalışmanın birinci kısmında, boron içeren oligotiyofenlerdeki tiyofen ve reaktif oksijen türleri arasındaki tepkimelerin analizi yapılmıştır. Bu çalışmada kullanılan reaktif oksijen türleri hidroksil radikali, hidroperoksil radikali, singlet moleküler oksijen ($^1O_2$) ve triplet moleküler oksijen ($^3O_2$) olarak listelenebilir. Her tepkime için geçiş durumu yapısı tespit edilmiştir. Her tepkime mekanizması için serbest enerji profili çizilmiştir.

Çalışmanın ikinci kısmında, hipergolik yakıtların yanma tepkimeleri değerlendirilmiştir. Yakıtlar ve nitrik arasında arasında gerçekleşen tepkimeler modellenmiştir. Başlangıç olarak tuz oluşumu çok egzotermiktir ve yanma tepkimeleri için enerji sağlar: H-koparma, β-ayrılma ve N-N_2 bağ fisyonu tepkimeleri bu enerji sayesinde gerçekleşmektedir. Tuz oluşumu tepkimelerinin tepkenleri ve ürünleri kapalı çözümlü olarak 298.15°C'de nitrik asitin içinde incelenmiştir. Diğer tepkimelerin geçiş durumu yapıları vakumda 423K'de tespit edilmiştir. Reaksiyon kinetiği analizleri ateşleme gecikmesi sürelerinin arasındaki farka ışık tutmaktadır.

TABLE OF CONTENTS

LIST OF FIGURES

LIST OF TABLES

LIST OF SYMBOLS

E_b	Binding energy
E_d	Dissociation energy
E_{el}	Electronic and zero-point energy
$E_c[\rho]$	Correlation energy
$E_{KE}[\rho]$	Kinetic energy
$E_x[\rho]$	Exchange energy
$E_{xc}[\rho]$	Exchange and correlation energy
$J[\rho]$	Coulomb energy
$T_s[\rho]$	Kinetic energy of non-interacting electrons
U_x^{σ}	Exchange energy density
$V_{\text{ext}}(\mathbf{r})$	External potential
V_{KS}	Kohn-Sham potential
ΔE_b	Relative binding energy
ΔE_d	Relative dissociation energy
ΔE_{el}	Relative electronic and zero-point energy
ΔE_{rxn}	Heat of reaction as electronic energy
ε_i	Kohn-Sham orbital energy
$v(r)$	External potential
$\rho(r)$	Electron density
ψ_i	Kohn-Sham orbitals
Ψ	Many electron wavefunction

LIST OF ACRONYMS/ABBREVIATIONS

B3LYP	Becke-3-parameter Lee-Yang-Parr functional
DFT	Density functional theory
DMAZ	2-azido-N,N-dimethylethan-1-amine
GGA	Generalized gradient approximation
$\hat{H}$	Hamiltonian operator
h_i	One-electron hamiltonian
HF	Hartree-Fock
HOMO	Highest occupied molecular orbital
IRFNA	Inhibited red fuming nitric acid
KS	Kohn-Sham
LDA	Local density approximation
M06-2X	Hybrid meta exchange-correlation functional
NPA	Natural population analysis
PCM	Polarizable continuum model
RMD	Reactive molecular dynamics
TMEDA	N, N, N', N'-tetramethylethylenediamine
WFNA	White fuming nitric acid

1. INTRODUCTION

This dissertation is made up of theoretical work on investigation of i) photo-active organic material regarding their photo-oxidative degradation and ii) fuel-oxidizer pairs of hypergolic propellants regarding their ignition delay times.

Boron-containing oligothiophenes have been proven to have exceptional optical properties [1–4]. For the commercialization and use of optically active organic materials, the photo-stability is fundamental. Under sunlight, the performance usually deteriorates due to nanoscale morphology degradation, thermo-oxidation and photo-oxidation of the active material and electrochemical degradation of active layer materials due to the diffusion of oxygen and water through the electrode/interlayer materials [5]. Among these degradation types photo-oxidative degradation is chosen to be assessed computationally. Reactions between the thiophene in the backbone and photo-generated reactive oxygen species such as hydroxyl radical, hydroperoxyl radical, singlet and triplet oxygen have been investigated. In Chapter 4, the free energy barriers of these reactions have been compared. These results will clarify the photostability, and hence the potential drawbacks of the large-scale use of this class of polythiophenes.

Hydrazine based fuels of hypergolic propellants are proven to be of high carcinogenicity [6]. Amine based fuels are scrutinized as more environment-friendly substitutes for hydrazine based fuels. However, amine based fuels lack in performance with respect to hyrazine based fuels. Ignition delay time measurements are used in the assesment of their performance [7]. An amine based fuel, TMEDA and an amine based fuel with an azide group, DMAZ have been chosen to understand the rationale underlying their ignition delay time difference. In Chapter 5, ignition reactions of TMEDA and DMAZ are compared pointing out the relationship between their structures and their performances.

2. THEORETICAL BACKGROUND

2.1. Density Functional Theory

Density Functional Theory (DFT), is a quantum mechanical method to estimate a solution to the Schrödinger equation for many electron systems [8, 9]. The aforementioned equation is based on the theorems of Kohn-Hohenberg which are proposed in 1964 [9]. The energy expression is supplied by the functional of electron density ρ(r), a function of time and space. Hence, electron density is the foundation of DFT. With respect to the wavefunction of many-electron system which is a function of 3N variables (the coordinates of all N number of atoms in the system), electron density is a functional of just three variables: the three spatial coordinates (x, y, z).

The definition of electron density is as follows [8];

$$\rho(r)=N\int\cdots\int|\Psi(r_1,r_2,\cdots,r_{next})|^2 dr_1 dr_2\cdots dr_n \qquad (2.1)$$

where *r* represents both spin and spatial coordinates of electrons. DFT expresses the energy in the two terms as a function of electron density;

$$E[\rho(r)]=\int V_{ext}(r)\,\rho(r)dr+F[\rho(r)] \qquad (2.2)$$

where $V_{ext}(r)\,\rho(r)dr$ describes the interaction of electrons with an external potential $V_{ext}(r)$, which is mainly the coulomb interaction with the nuclei. Nonetheless, the term $F[\rho(r)]$ represents the sum of the kinetic energy of electrons and the contribution from interelectronic interaction [8].

In 1965, Kohn and Sham have made significant contributions to density functional theory by introducing a new approach to the problem with equation 2.2 which was undefined F[ρ(r)]. The improvement of the equation is achieved by tackling F[ρ(r)] function as a sum of three terms;

$$F[\rho(r)]=E_{KE}[\rho(r)]+J[\rho(r)]+ E_{XC}[\rho(r)] \quad (2.3)$$

where $E_{KE}[\rho(r)]$ is the kinetic energy of the non-interacting electrons, $J[\rho(r)]$ is the electron-electron coulombic energy which is otherwise called Hartree electrostatic energy. $J[\rho(r)]$ is the sum of pairwise electrostatic energy between two charge densities and $E_{XC}[\rho(r)]$ is the exchange-correlation energy including the contribution of exchange and correlation, also the kinetic energy difference between interacting (true kinetic energy of the system) and non-interacting electrons ($E_{KE}[\rho(r)]$). Accordingly, the sum of exchange $E_X[\rho(r)]$ and correlation $E_C[\rho(r)]$ functionals is $E_{XC}[\rho(r)]$.

Kohn Sham density functional theory defines Kohn-Sham equation as the one-electron Schrödinger equation of a reference non-interacting particle system which generates the same density as any given system of interacting particles. The Kohn-Sham wavefunction, a single Slater determinant generated by a set of independent orbitals, Ψ_i, serves as the lowest energy solution to Kohn-Sham equations.

$$\left[-\frac{1}{2}\nabla^2+V_{KS}\right]\Psi_i=\varepsilon_i\Psi_i \quad (2.4)$$

Here, ε_i describes the Kohn-Sham orbital energy. Local external Kohn Sham potential, V_{KS}, in which the non-interacting particles move, defines The Kohn –Sham equation (2.4).

$$V_{KS}= v(r)+\frac{\partial J[\rho]}{\partial\rho(r)}+\frac{\partial E_{XC}[\rho]}{\partial\rho(r)} \quad (2.5)$$

$$V_{KS}= v(r)+\frac{\rho(r')}{|r-r'|}dr' +v_{XC}(r) \quad (2.6)$$

Here, $v_{XC}(r)$ defines the exchange-correlation potential. The density for an N-particle system is;

$$\rho(r)=\sum_i^N |\Psi_i|^2 \quad (2.7)$$

if the exchange-correlation functional's definite form is known. Nevertheless, this functional's definite form is unknown. Thus, exchange-correlation functionals are being developed.

2.2. General Approach to Exchange-Correlation Density Functionals

The exchange-correlation effect assumes that electrons are interacting particles. Since the wave function of electron depends on the position and spin momentum of other electrons in the system, electrons stand at a certain distance to each other so that coulomb repulsion is diminished. In order to include the inhomogeneity of the electron gas as a function of the interelectronic distance r' and the electron density, $\rho(r')$, exchange-correlation density functional is developed. Electrons with the same spin being close to each other, which is also called exchange-correlation hole, is prevented by an interaction potential. Thereby Coulomb repulsion obstacle is overcome.

Density functionals, tackle electron-exchange and electron-correlation assumptions on an individual basis. Wrong assumptions arise from the separation for the known exact form of the exchange operator (from the Hartree-Fock theory) and the exchange operator for a homogeneous electron gas are non-identical [10]. The implementation of previous parametrization of these models improves the exchange and correlation density funtionals to achieve different observables determined from experiment and highly accurate HF calculations, such as vibrational spectra, reaction energies, atomization energies. [10].

The exchange and correlation functionals define the volume of the N electrons by a regular grid which evaluates the electron density to show it as a numerical value. Thus, when valence electrons are considered, the electron density calculation along the grid fails as the exact electron density and the homogeneous electron gas approximation contradict each other. The specific expression of self-iteraction energy is derived from Coulomb's repulsion

between Kohn-Sham orbitals and the electron density cannot be derived even though exchange-correlation functionals provide exceptional enhancements. As a result of the non-local nature of electron-exchange, the exchange-density functional is not entirely adequate to express the self-interaction in the uniform electron gas system [17-19]. This obstacle is overcome by combining the non-local exchange operator from Hartree Fock theory and exchange density functional. Relying on the accuracy of the calculation against high-level ab initio methods or the experimental data sets the extent of HF exchange is determined [18, 19]. Including HF exchange functional to the GGA and meta-GGA density functionals facilitates the calculation with high accuracy just as formerly maintained by HF methods but with a reduced computational cost.

Additional knowledge of the local interaction of the Kohn-Sham orbitals with the electron density is brought in because the exchange, v_X and correlation, v_C operators of the local density approximation (LDA), are inadequate to convey local exchange-correlation energy of the system. In the exchange-correlation density functional, the improvement is accomplished by including the gradient of the electron density. The GGA functional includes only the electron density and its first derivative whereas the meta-GGA functional includes second derivative of electron density additional to the density and its first derivative in the exchange correlation potential.

$$v_{XC} = E_{XC}[\rho(r')] + \Delta E_{XC}[\rho(r'),\nabla\rho(r')] + \Delta\Delta E_{XC}[\rho(r'),\nabla\rho(r'),\nabla^2\rho(r')] \quad (2.8)$$

Hybrid-GGA and meta-GGA functionals are improved versions of GGA functionals. The combination of the exchange correlation of GGA and HF exchange is used to develop hybrid density functionals [12].

In this thesis, M06-2X hybrid functional, introduced by Zhao *et al.*, is used,

$$E_{XC}^{hyb} = \frac{X}{100} E_X^{HF} + \left(1 - \frac{X}{100}\right) E_X^{DFT} + E_C^{DFT} \quad (3.9)$$

For M06-2X functional, X, the percentage of Hartree-Fock exchange, is taken as 54 [13].

2.3. Basis Sets

The electronic wavefunction in DFT is represented by a basis set, which is a set of one particle functions. Linear combinations of LCAO-MO approximation is used to express molecular orbitals.

$$\phi_i = \sum_{\mu=1}^{K} c_{\mu i} f_\mu \tag{2.10}$$

where the functions ϕ_i , f_μ and $c_{\mu i}$ represent molecular orbital, atomic orbital and coefficients, respectively. Total number of atomic orbital functions is denoted with K.

Pople has introduced split-valence basis sets to reduce the computational cost. Hence computational chemistry employs them extensively. Split-valence basis sets utilize two different basis sets to tackle core electrons and valence electrons of an atom. This is based on the fact that the core electrons are more stable against the environment than the valence electrons. In that respect, the core electrons use a smaller basis set than the valence electrons. Case in point, 6-21+G, 6-31G* and 6-311++G are some of the Pople basis sets. The number of Gaussian functions used for the core orbitals is the number on the left hand-side of the dash and the numbers of Gaussian functions used for the valence orbitals are the numbers on the right hand-side. Number combinations of two digits and three digits signify valence double-ζ basis and valence triple-ζ basis, respectively. Diffuse functions and/or polarization functions are included to extend the basis sets [14].

Polarization functions add higher angular momentum to atoms. If polarization functions are just added for all the heavy atoms, they are denoted by either "*" or "(d)". If hydrogen atoms are also considered, they are denoted by either "**" or "(d,p)".

The effect of the atom on the core electrons of another atom,which is far away from the atom, is included by the addition of diffuse functions. Diffuse functions allow orbitals to cover more space. A single "+" sign implies the inclusion diffuse functions for heavy atoms, whereas the second "+" sign adds the diffuse functions for the light atoms.

2.4. Continuum Solvation Models

Solvation effects are introduced to quantum mechanical calculations by continuum solvation models. Describing the system in a continuous approach through a distribution function results in the reduction of the number of degrees of freedom [23, 24].

Continuum solvation models use a polarizable medium which serves as the solvent in the system. Since the dielectric medium surrounds the cavity in which the solute is embedded, static dielectric constant ε is one the main descriptors of the dielectric medium.

The total solvation free energy is calculated by,

$$\Delta G_{solvation} = \Delta G_{cavity} + \Delta G_{dispersion} + \Delta G_{electrostatic} + \Delta G_{repulsion} \quad (2.11)$$

where ΔG_{cavity} signifies the cost of placing the solute in the medium in terms of Gibbs energy. $\Delta G_{dispersion}$ stabilizes solvation free energy and adds the dispersion interactions between solute and solvent. $\Delta G_{electrostatic}$ represents the electrostatic part of the solute-solvent interaction energy. $\Delta G_{repulsion}$ includes the exchange solute-solvent interactions which were not a part of the cavitation energy.

The electrostatic problem is the fundamental issue of continuum solvation models, which given by the Poisson equation:

$$-\vec{\nabla}\left[\varepsilon(\vec{r})\nabla\vec{V}(\vec{r})\right] = 4\pi\rho_M(\vec{r}) \quad (2.12)$$

reduced to

$$-\nabla^2 V(\vec{r}) = 4\pi\rho_M(\vec{r}) \text{ within } C \quad (2.13)$$

$$-\varepsilon\nabla^2 V(\vec{r}) = 0 \text{ outside } C \quad (2.14)$$

where C is the part of space occupied by cavity, ε is dielectric function, V is the sum of electrostatic potential V_M generated by the charge distribution ρ_M and the reaction potential V_R generated by the polarization of the dielectric medium:

$$V(\vec{r}) = V_M(\vec{r}) + V_R(\vec{r}) \tag{2.15}$$

The Polarizable Continuum Model (PCM) is one of the polarizable continuum solvation models [17]. Solute is embedded in a cavity, which is described by a set of spheres centered on atoms with radii based on the van der Waals radius. Then subdivision of the cavity surface into small domains, in which polarization charges are put, is performed. Three distinct ways of employing PCM calculations are possible. Dielectric PCM (D-PCM) is the original method. The second model, conductor-like PCM (C-PCM), models the encircling medium as a conductor rather than a dielectric [18]. The third model, integral equation formalism PCM (IEF-PCM), recasts the PCM equations in an integragral equation formalism by implementation [27, 28]. PCM is used in this work.

3. THE PHOTO-OXIDATIVE DEGRADATION MECHANISMS OF THIOPHENE IN BORON-CONTAINING OLIGOTHIOPHENES

3.1. Introduction

Among the class of heterocyclic compounds, thiophene is one of the most widely investigated starting material, on account of various advantages. First of all, thiophene's fabrication as a by-product of crude oil distillation makes it inexpensive. Thiophene is also known to be chemically stable and easy to process. Moreover, the fine-tuning of thiophene-based materials' desirable properties is achievable by means of its chemical functionalization. However, there is a clear relation between thiophene structure and properties even if improving is far from being complete, and hence novel thiophene-based materials are constantly designed, synthesized and characterized [21–23]. The thiophene structure is used in compounds of many diverse fields ranging from organic material science to pharmaceutical applications. Furthermore, oligothiophenes and polythiophenes are generally studied for their optoelectronic properties which can be used in semiconductors such as organic field effect transistors [24, 25], light-emitting diodes [26-27], and photovoltaic cells [28–30].

Considering thiophene-based materials, the incorporation of three-coordinated boron to the π-conjugated organic systems is possible and advantageous due to boron's vacant p orbital which makes it acting as a π-acceptor whilst remaining a σ-donor; hence boron assists the extension of conjugation in π-conjugated organoboranes. As the boron center is susceptible to nucleophilic attack by water vapor and other oxidative species found in air, bulky aryl groups are used as substituents to supply steric protection against oxidation of the three-coordinated boron. The mesityl (2,4,6-trimethylphenyl) group can be cited as an example of a bulky substituent [4, 31]. Hence, although boron is protected by the presence of bulky groups, thiophene rings remain exposed to solvent and are prone to be degraded by oxidative species.

Boron containing oligothiophenes have been previously investigated for their use in optoelectronic devices and organic light-emitting diodes (Figure 3.1.). Shirota *et al.* have shown that 5,5′-bis(E-dimesitylboryl)-2,2′-bithiophene (BMB-2T), and 5,5′-bis(Edimesitylboryl)-2,2′:5′,2″-terthiophene (BMB-3T) can be used as thermally stable, electron-transporting amorphous materials to form green light emitting diodes with tris(8-quinolinolato)aluminum(Alq_3). Since BMB-2T is an electroluminescent material absorbing with maximum wavelengths of 446 nm and 472 nm, it is also used as blue-emitting amorphous molecular material in blue OLED devices [1–3]. Furthermore, two-photon absorption (TPA) capabilities of these molecules have been investigated computationally [32], and experimentally [4] highlighting large cross-sections in the infrared region. Entwistle *et al.* have found that among the structures investigated, 5,5′-bis(E-dimesitylborylethenyl)-2,2′:5′,2″-terthiophene (BMBE-3T) has a maximum two-photon absorption cross-section of *ca* 1800 Göppert-Mayer (GM) which occurs *ca* 800 nm (Figure 3.1.) [4].

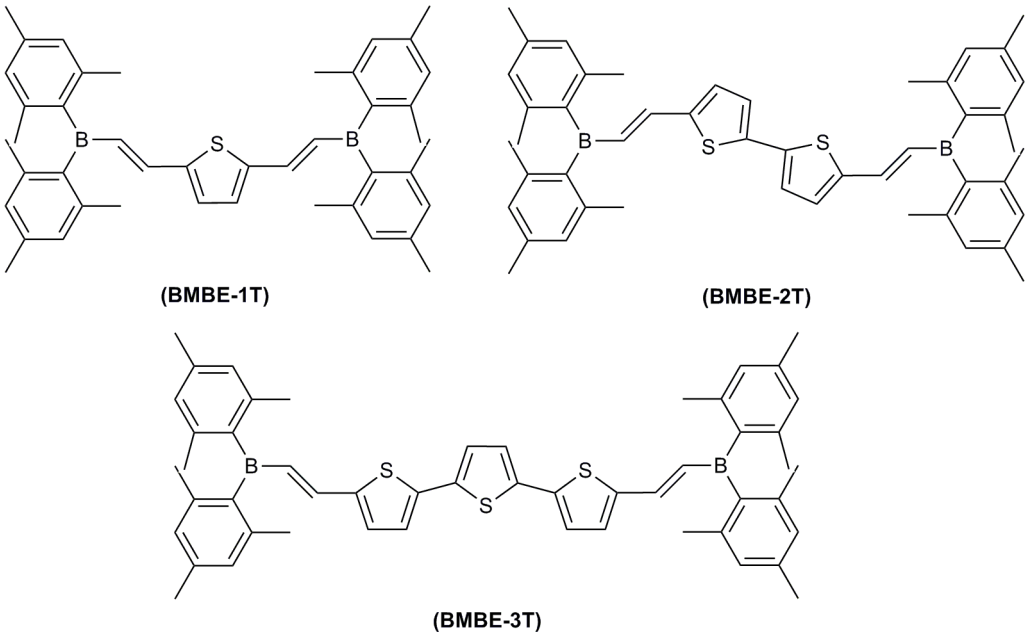

Figure 3.1. Chemical formulas of the investigated (E-dimesitylborylethenyl)-substituted arenes. (BMBE-1T) 2,5- bis(E-dimesitylborylethenyl)thiophene, (BMBE-2T) 5,5′-bis(E-dimesitylborylethenyl)-2,2′-bithiophene, (BMBE-3T) 5,5′-bis(E-dimesitylborylethenyl)-2,2′:5′,2″-terthiophene.

However, optically active organic materials come across two problems on their way to commercialization: efficiency and stability. Even though the efficiency of organic materials is rapidly increasing, the performance loss over time is generally unavoidable [33]. Thus analysis of the possible oxidative degradation pathways of this set of organic materials is crucial for the classification of the stability issues and further design of more stable boron containing oligothiophenes.

The oxidation mechanisms of the thiophene ring by reactive oxygen and nitrogen species (ROS, NOS) such as •OH [34–36], O_3 [35], NO_3 [37–39] radicals and $^1O_2$, $^3O_2$ [40] have been broadly studied through experiments and computation. Obviously the ground state triplet molecular oxygen is found to be the most abundant ROS present in operating conditions, yet Song *et al.* have shown that the energetic barrier for any reaction between thiophene and triplet molecular oxygen is much higher than the one between thiophene and singlet molecular oxygen [40]. On the other hand, Sengul et al. have shown that thiophene containing dyes (2,5-dithienylpyrrole: DPT1 and DPT2) are able to act as photosensitizers capable of generating singlet molecular oxygen due to the efficient intersystem crossing of these systems [23]. The fast and relatively efficient triplet manifold population of mono- and poly-thiophene compounds has also been confirmed using non-adiabatic molecular dynamics (NAMD) and the ring-opening is due to the photo-induced enlargement of the carbon-sulfur bond [21, 22]. Hence, taking into account the role of singlet oxygen in thiophene degradation pathways is crucial. Furthermore, certain degradation mechanisms with •OH and O_2 have been suggested by experimental [41–43] and computational studies of poly(3-hexylthiophene-2,5-diyl) (P3HT).

In the present study, a set of boron containing oligothiophenes, varying only by the number of thiophene rings in the backbone, is chosen to investigate the oxidative degradation mechanisms undergone by the thiophene ring. The chemical mechanisms considered in this study are reported in Figure 3.2.; the degradation mechanisms 1, 2Xa and 2Xb have been suggested for P3HT, while mechanisms 3a, 3b and 3c have been selected based upon the computational study of the oxidative degradation of a thiophene molecule by $^1O_2$, $^3O_2$ for their low barriers [40].

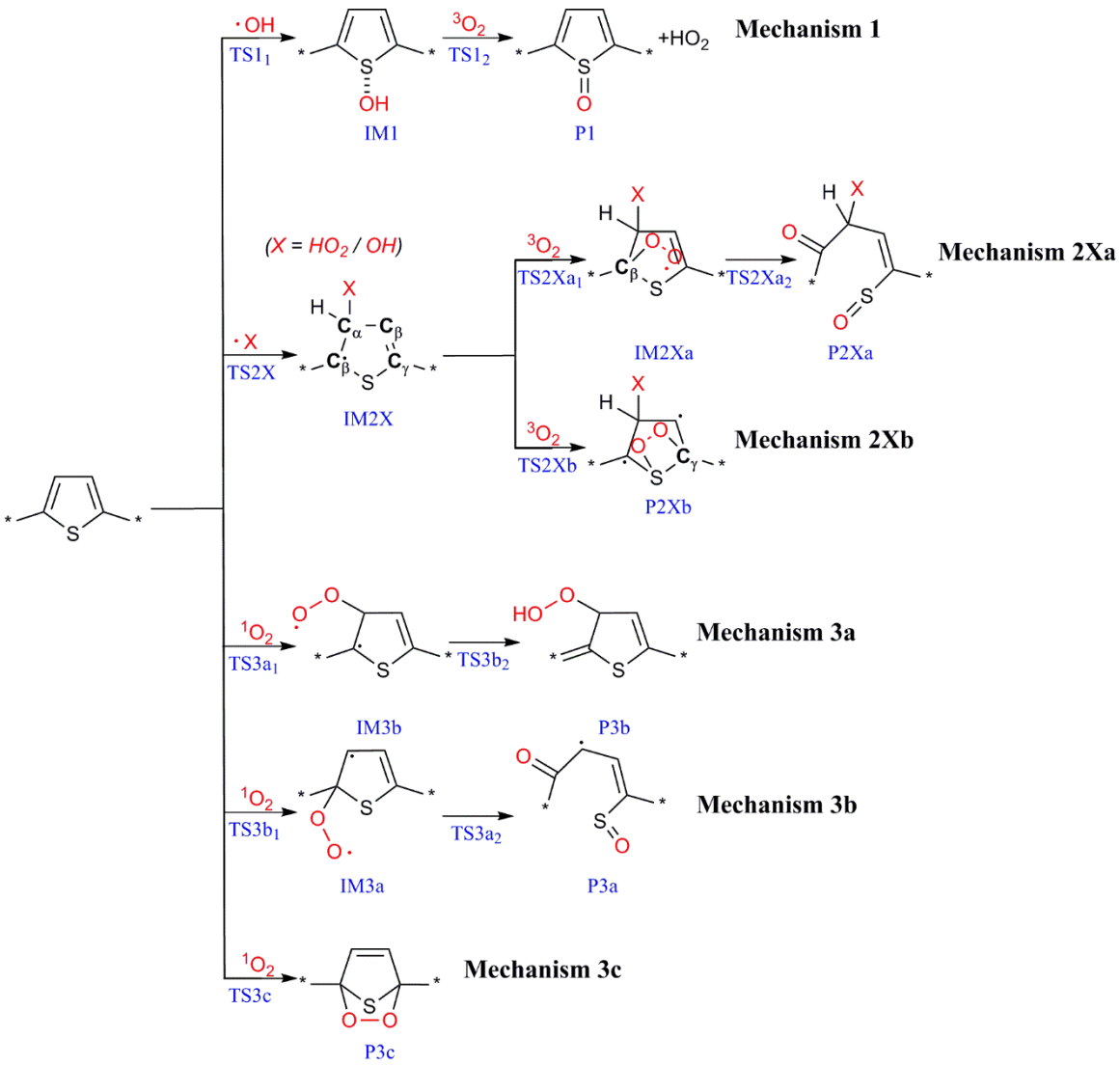

Figure 3.2. Oxidative Degradation Pathways for Thiophene Ring of Boron Containing Oligothiophenes

Thereby our goal is to address three questions: first, which reaction mechanism is the most possible degradation route for this set of boron containing oligomers, then how boron affects the stability of the whole structure, and finally, what the role of the number of thiophene rings on the stability of these species is.

3.2. Computational Methodology

The reported calculations have been carried out with Gaussian E09 software package employing density functional theory (DFT). Harmonic vibrational frequency calculations and

geometry optimizations of the ground state and transition state structures are carried out in vacuum using the B3LYP functional [44] and standard Pople basis sets: 6-31G(d) for carbon, hydrogen, oxygen, boron, and 6-311++G (3df,3pd) for sulfur. Unrestricted approach has been applied for the open-shell species while restricted approach is applied for the closed-shell species.

Open-shell species are checked for spin contamination. Geometries corresponding to local minima have been confirmed to lack imaginary vibrational frequencies whereas transition state structures have a single imaginary frequency. Conformational search for the stationary points has been carried out around each single bond. Intrinsic reaction coordinate (IRC) calculations have been carried out for the transition state structures in order to scrutinize the validity of each one.

3.3. Results and Discussion

In order to minimize the computational costs, small model systems are proposed (Figure 3.3.) keeping the main functional groups of the parent compound, also allowing to assess the influence of the different chemical groups on the overall reactivity. In Figure 3.4. 3-dimensional structures of the investigated molecules are listed.

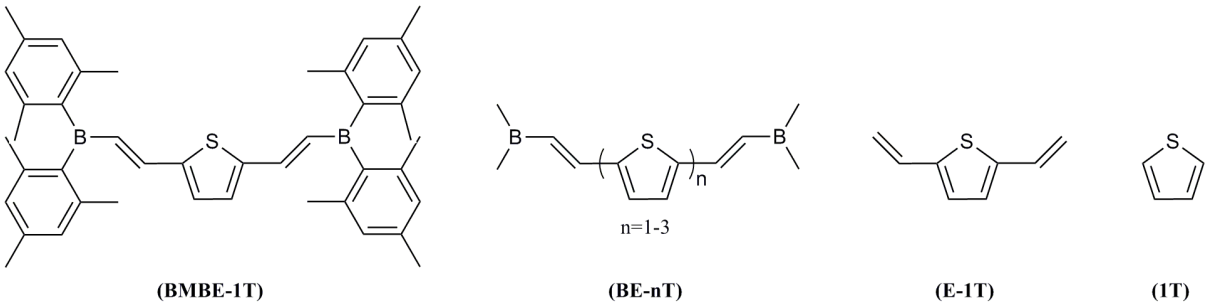

Figure 3.3. Chemical formulas of the investigated molecules: **(BMBE-1T)** 2,5- bis(*E*-dimesitylborylethenyl)thiophene, **(BE-1T)** 2,5- bis(*E*-dimethylborylethenyl)thiophene, **(E-1T)** 2,5- bis(ethenyl)thiophene, **(1T)** thiophene.

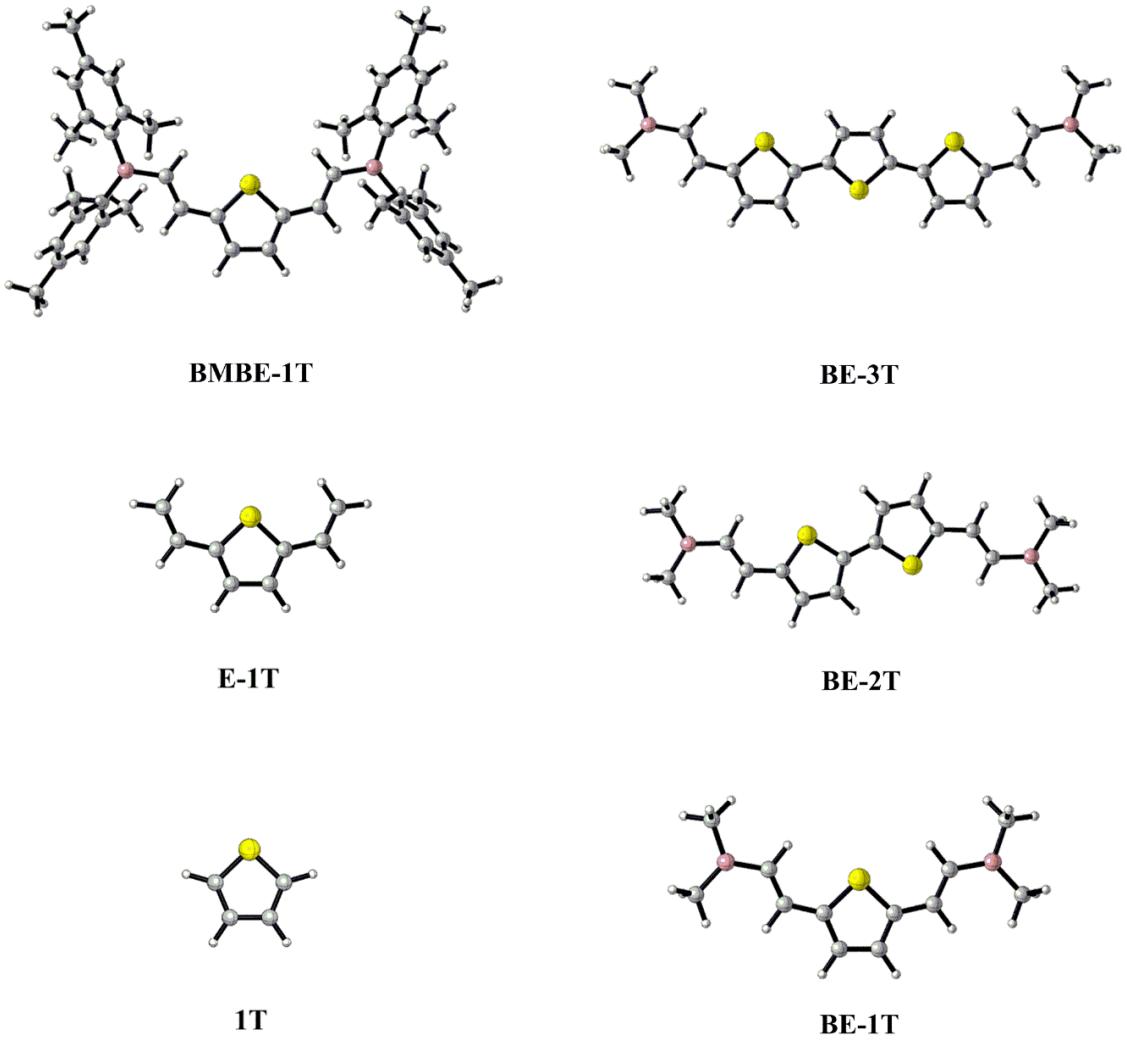

Figure 3.4. Optimized structures of reactants (B3LYP/6-31G(d) for H, C, N, O and 6311++G (3df,3pd) for S in vacuum).

3.3.1. Mechanism 1: Sulfoxide Formation

Initially addition of OH radical (Mechanism 1) is explored. In their computational study, Sai *et al.* have stated that SOH adduct of P3HT is thermodynamically unstable and its formation is endothermic in nature [45]. As reported in Figure 3.5., H abstraction by triplet molecular oxygen ($^3O_2$) from the BMBE-1T(S)-OH adduct has a free energy barrier of 7.2 kcal·mol^{-1} and it is slightly exergonic with free reaction energy of -1.3 kcal·mol^{-1}. Hence it is found to be kinetically and thermodynamically favorable.

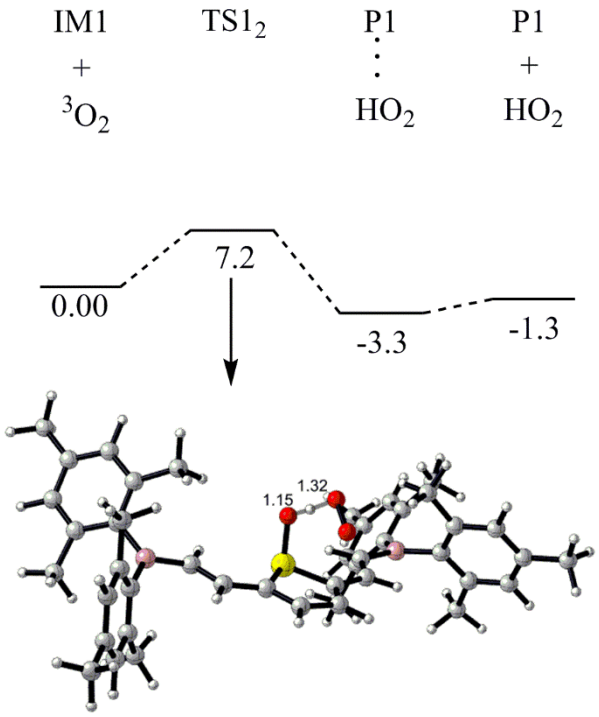

Figure 3.5. Gibbs energy profile (kcal·mol^{-1}) for Mechanism 1 for BMBE-1T. (B3LYP/6-31G(d) for H, B, C, O and 6-311++G(3df,3pd) for S)

Table 3.1. Gibbs energies of activation ($\Delta G^{\neq}$), Gibbs energies of reaction (ΔG_{rxn}) (kcal·mol^{-1}) for Mechanism 1_2 and distances (Å) for $TS1_2$ (B3LYP/6-31G(d) for H, B, C, O and 6-311++G(3df,3pd) for S).

	BMBE-1T	BE-1T	E-1T	1T	BE-1T	BE-2T	BE-3T
$\Delta G^{\neq}$	7.2	7.7	9.9	11.7	7.7	7.8	7.0
ΔG_{rxn}	-1.3	-1.9	-1.6	0.1	-1.9	-2.9	-4.5
$H\text{-}O_{IM1}$	1.15	1.13	1.11	1.13	1.13	1.12	1.11
$H\text{-}O_{O=O}$	1.32	1.34	1.39	1.36	1.34	1.37	1.38

As shown in Table 3.1., among the small molecules BE-1T shares similar results with BMBE-1T in terms of free energy of activation. Free energy of reaction results of BE-1T and BMBE-1T are -1.9 kcal·mol^{-1} and -1.3 kcal·mol^{-1}. Regarding reaction 1_2, substitution of mesityl groups of BMBE-1T with hydrogens to form BE-1T does not cause considerable difference in free energies of activation and reaction. Hence, the free energy profiles of BE-1T, BE-2T, and BE-3T can be used to account for BMBE-1T, BMBE-2T and BMBE-3T. Interestingly enough,

there's no significant difference between the free activation energies of BE-1T and BE-2T whereas the free activation energy of BE-3T is slightly lower than the other two. Moreover among the species BE-1T to BE-2T and BE-3T we observe a significant decrease in the free energy of reaction. Thus, one can foresee that larger aggregates will be more prone to degrade by the combined effect of radicals and triplet oxygen.

The role of boron is investigated by substituting the dimethylboryl substituents in BE-1T with hydrogens in E-1T. For reaction 1_2, the Gibbs activation energy is found to be 9.9 kcal·mol^{-1} for E-1T and 7.7 kcal·mol^{-1} for B-1T and its Gibbs energy of reaction is 0.3 kcal·mol^{-1} higher for BE-1T than for E-1T. E-1T is kinetically less reachable and the product is thermodynamically slightly less stable than in the case of BE-1T, hence the presence of boron seems to play a protective role against degradation.

Overall degradation by sulfoxide oxidation is slightly facilitated by the presence of dimesitylborylethenyl and borylethenyl groups.

In Figure 3.6., Figure 3.7. and Figure 3.8. $\langle S^2 \rangle$ values are given in parenthesis. Since they are close to 0.75, spin contamination can be ruled out.

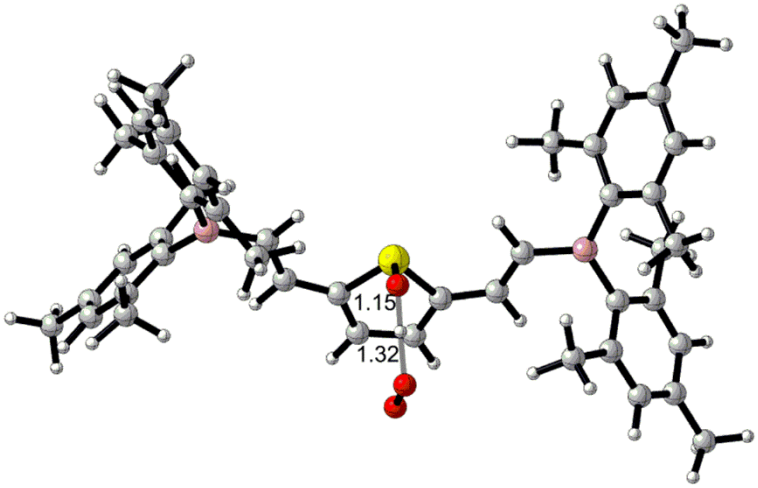

TS1 (0.7514)

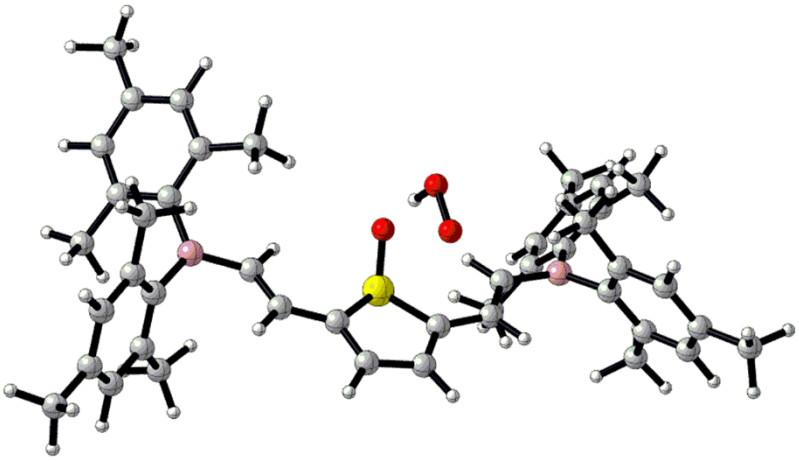

P1...HO_2 · (0.7500)

Figure 3.6. Optimized structures of TS1, and P1...HO_2• for BMBE-1T (B3LYP/6-31G(d) for H, C, N, O and 6-311++G(3df,3pd) for S in vacuum).

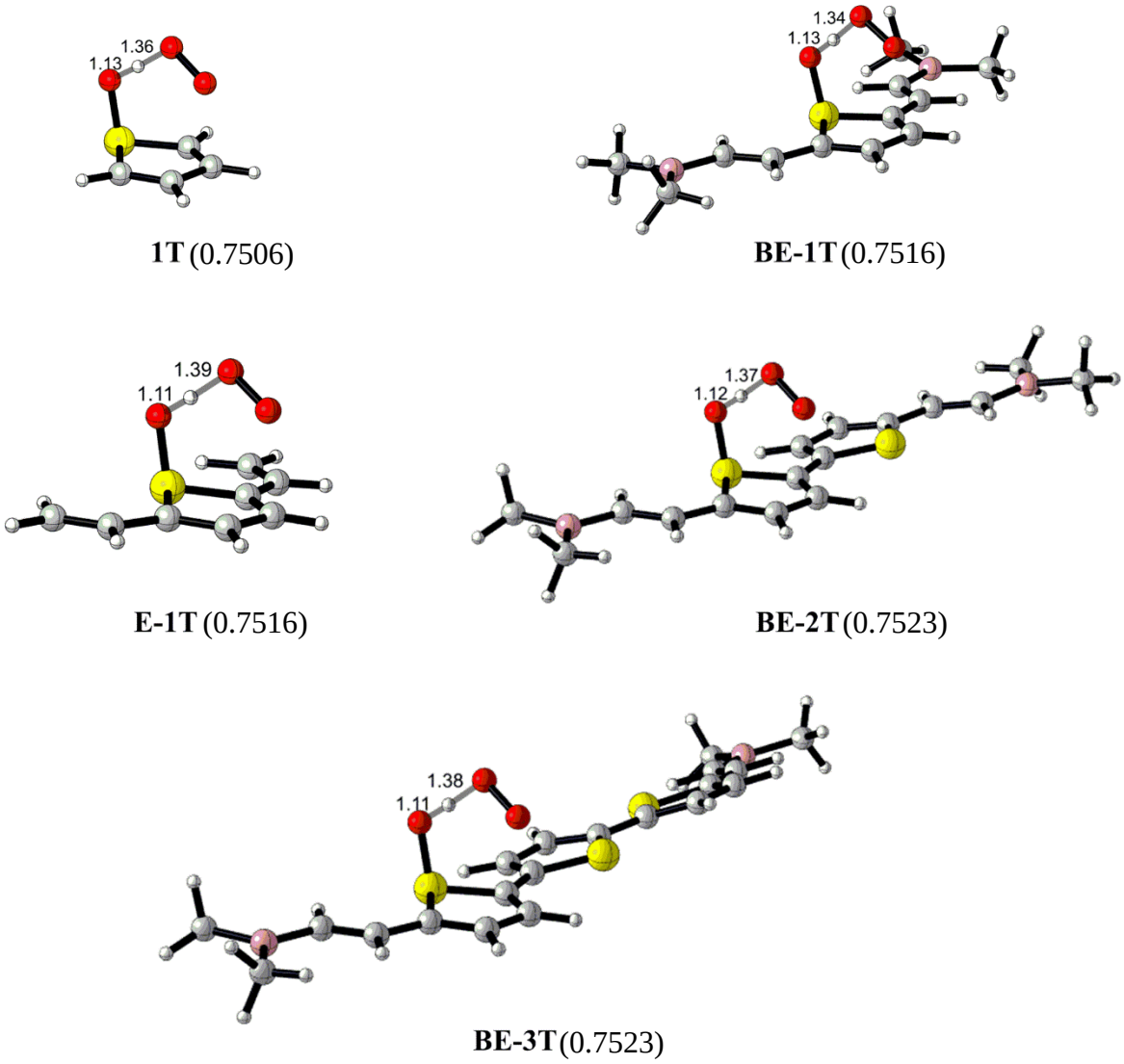

Figure 3.7. Optimized structures of $TS1_1$ (B3LYP/6-31G(d) for H, C, N, O and 6-311++G(3df,3pd) for S in vacuum).

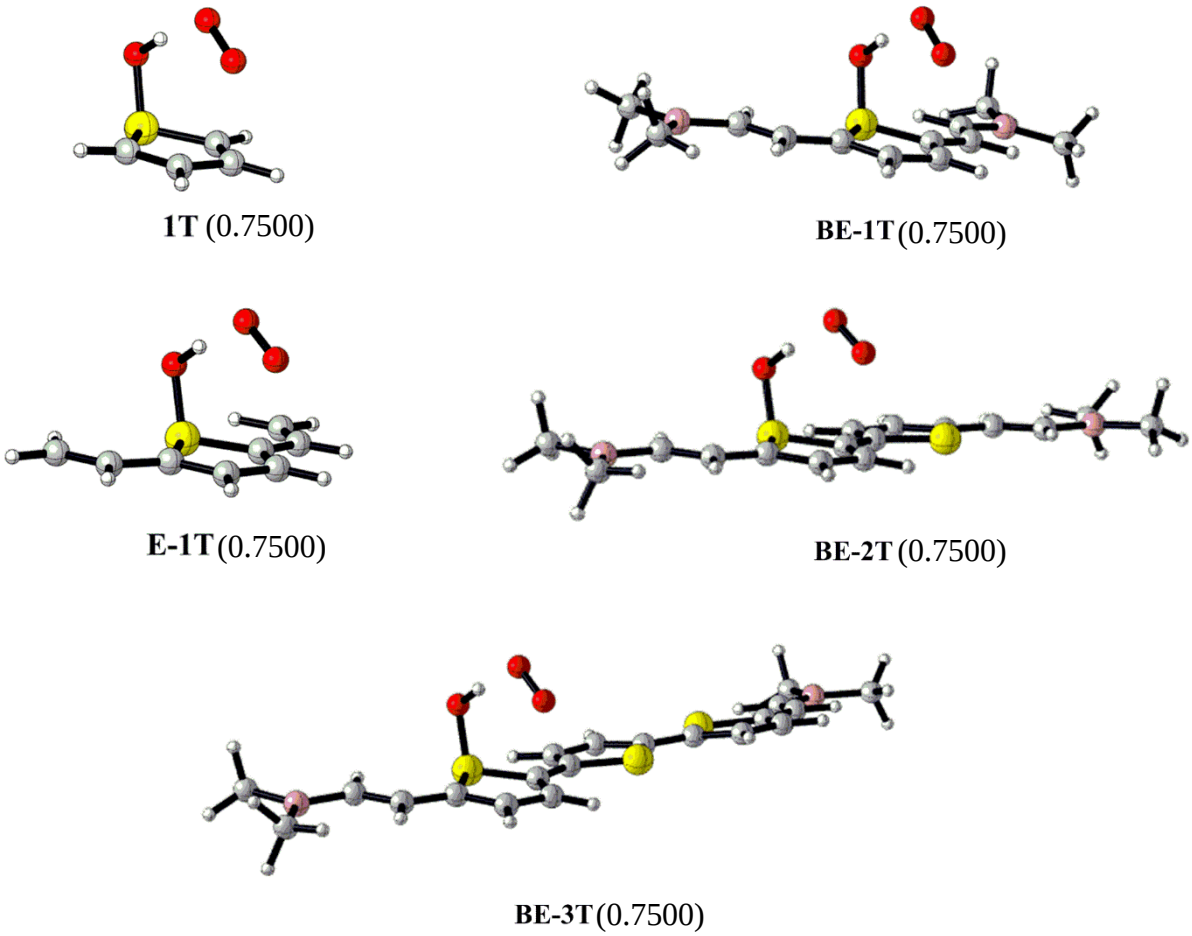

Figure 3.8. Optimized structures of P1...HO_2• (B3LYP/6-31G(d) for H, C, N, O and 6-311++G(3df,3pd) for S in vacuum).

3.3.2. Mechanisms 2Xa and 2Xb: Sequential Addition Pathways

The attack by ROS, and especially OH radical, on α and β positions of thiophene rings has been studied experimentally and theoretically. Furthermore, the same type of reaction has also been investigated for polythiophenes, such as P3HT, in order to identify the possible degradation pathways of organic photovoltaic devices. For instance, Sai *et al.* have reported that the P3HT(C)-OH adduct is thermodynamically more favorable than the P3HT(S)-OH adduct, by using the PBE0 functional and the P3BT supercell. Furthermore, the OH radical attack on the β carbon was found to be kinetically more favorable than the attack on the α carbon of the thiophene ring in P3HT [45].

However, since •OOH may form as a by-product from reactions in Mechanism 1 or other degradation reactions that may occur in the device, this radical can be considered to take part in the degradation process as well, and hence we have also modeled its reactivity.

After the addition of hydroxyl or hydroperoxyl radicals, subsequent O_2 attack can, in principle, take place in two possible ways: O_2 may attack the β carbon to the hydroxyl/hydroperoxyl moiety and the sulfur in a stepwise mechanism leading to ring opening as shown in mechanism 2Xa. Alternatively, O_2 may attack the γ carbon of the hydroxyl/hydroperoxyl moiety and the sulfur in a concerted manner (Mechanism 2Xb). O_2 attack on the γ carbon to the hydroxyl/hydroperoxyl moiety and the sulfur in a stepwise mechanism leading to ring opening has also been considered. However, the stepwise addition of O_2 to the γ carbon to the hydroxyl/hydroperoxyl moiety and the sulfur, does not seem to occur because, as can be seen by the analyses of the frontier molecular orbitals, the electronic density is not localized over the carbon which is going to be attacked by O_2. The HOMO wave function is not localized over the γ carbon to the hydroxyl moiety in IM2HO$_2$ (Figure 3.9.) .

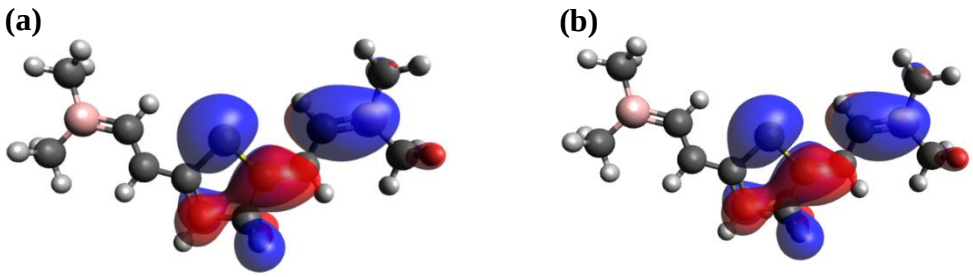

Figure 3.9. HOMO wavefunctions of B-1T on a) IM2OH, and b) IM2HO$_2$ (B3LYP/6-31G(d) for H, C, N, O and 6-311++G(3df,3pd) for S).

In this section, we will be discussing the 4 different sequential addition pathways for the three molecules BMBE-1T, BMBE-2T and BMBE-3T. Once again, to reduce the computational cost, we have substituted mesityl groups of aforementioned molecules with methyl groups in BE-1T, BE-2T and BE-3T. Thereby our aim is to find a plausible model for the bulky BMBE-1T,

BMBE-2T and BMBE-3T molecules by comparing the free energy profiles of BMBE-1T, BE-1T, BE-2T, and BE-3T.

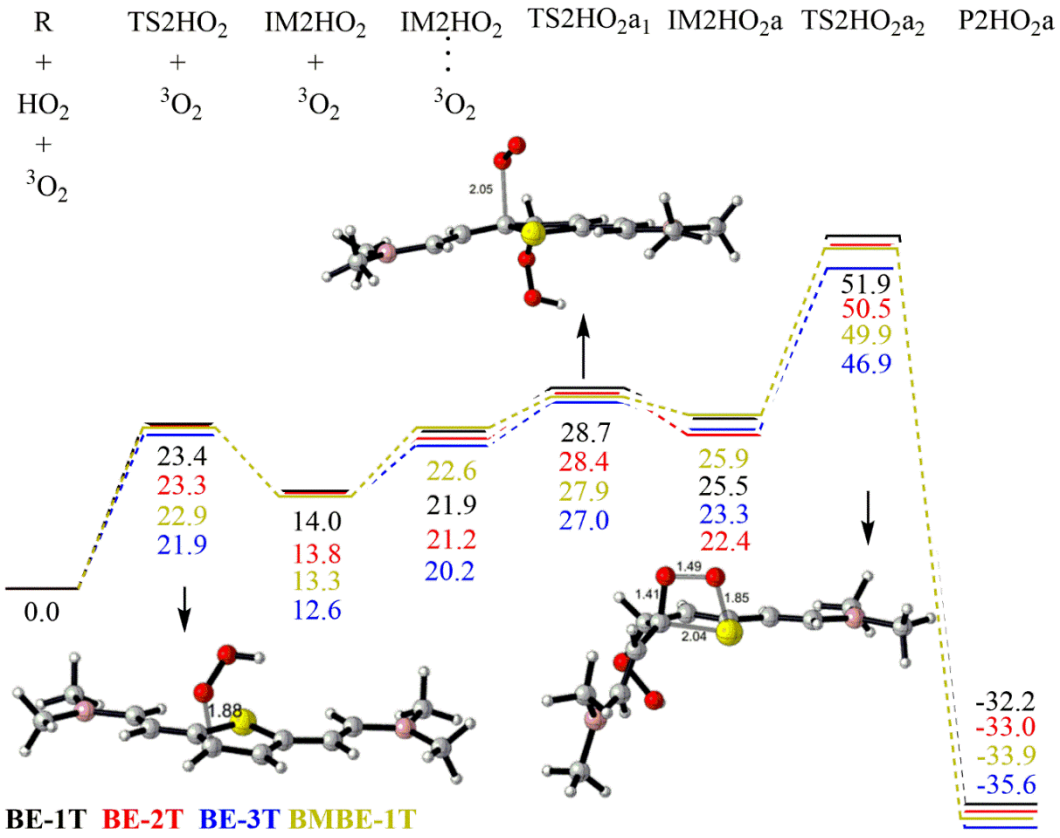

Figure 3.10. Gibbs energy profile (kcal·mol^{-1}) for Mechanism 2HO$_2$a for BE-1T, BE-2T, BE-3T, and BMBE-1T. (B3LYP/6-31G(d) for H, B, C, O and 6-311++G(3df,3pd) for S)

Among the 4 different pathways in this section, Mechanism 2HO$_2$a, i.e. the attack of triplet oxygen to the HO$_2$-functionalized thiophene, is modeled to understand whether the free energy profile for BMBE-1T is similar to the ones for BE-1T. Indeed, considering the differences in activation energies one can assess that globally the potential energy surfaces for BMBE-1T and BE-1T are very similar, while 1T follows a thermodynamically less stable path. Note that for compound 1T, TS2HO$_2$a$_1$ could not be located. Overall we concluded that BE-1T is a competent model for BMBE-1T (Figure 3.10.).

At this stage the role of thiophene rings has been investigated by considering the models BE-1T, BE-2T, and BE-3T (Figure 3.10.). Observation of the free energy barriers and the

thermodynamic features of the degradation of BE-1T, BE-2T and BE-3T reveals the fact that regardless of the number of thiophene rings the mechanism $2HO_2b$ proceeds with globally the same energetic requirements for BE-1T, BE-2T, and BE-3T.

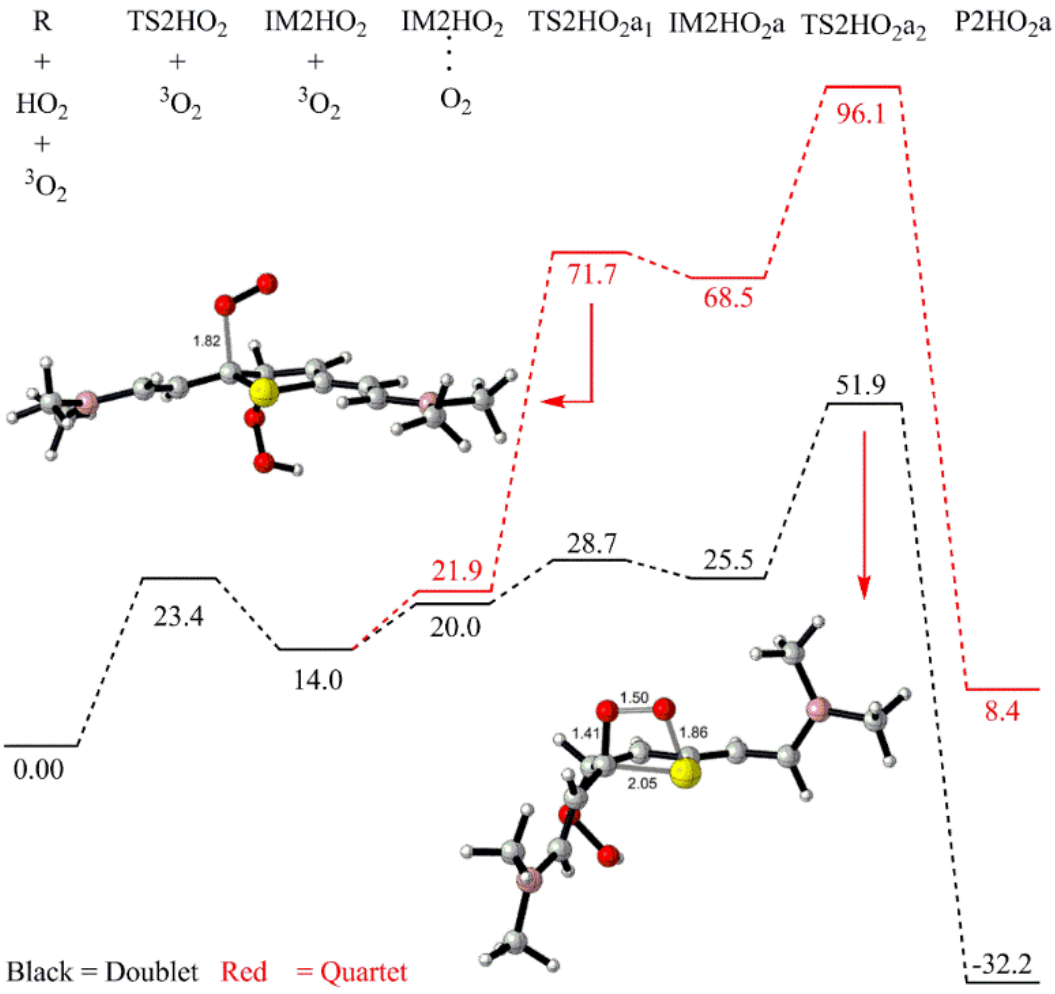

Figure 3.11. Free energy profile (kcal·mol^{-1}) for Mechanism 2HO2b for BE-1T in doublet and quartet systems. (B3LYP/6-31G(d) for H, B, C, O and 6-311++G(3df,3pd) for S)

Triplet oxygen attack on the intermediate, $IM2HO_2a$ can occur via either doublet or quartet manifold. Thus, the quartet system is also investigated for mechanisms $2HO_2a$. As shown in Figure 3.11., in the quartet state system, the first step of the stepwise reaction, $2Xa_1$, has a Gibbs free energies of activation of 57.7 kcal·mol^{-1} which is more demanding than that in the doublet state (14.7 kcal·mol^{-1}). However the Gibbs energy of activation and Gibbs energy of reaction

values of the second step do not change much between the doublet and the quartet states. It is 26.4 kcal·mol^{-1} for the doublet system and 27.6 kcal·mol^{-1} for the quartet system. One can observe that C-$O_{O=O}$ distance in transition state structure of the reaction $2HO_2a_1$ is 1.82 Å in the quartet energy level and 2.05 Å in the doublet energy level. $TS2HO_2a_2$ does not show significant difference between doublet and quartet systems. Thus, even if the second step of the stepwise $^3O_2$ attack has similar free energies of activation for doublet and quartet multiplicity, the first step clearly shows the difference.

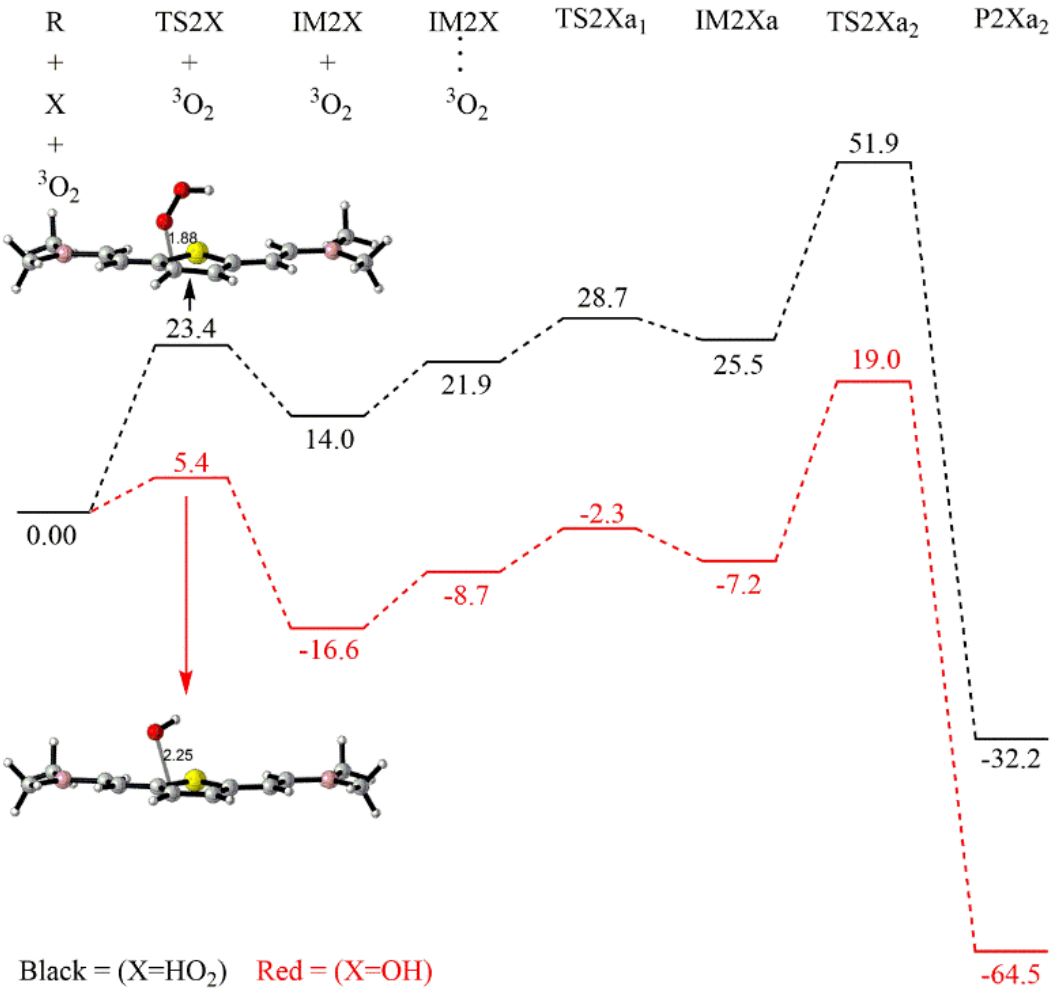

Figure 3.12. Free energy of activation ($\Delta G^{\neq}$) and free energy of reaction (ΔG_{rxn}, kcal·mol^{-1})for Mechanisms $2HO_2a$ and 2OHa for BE-1T. The mechanism for $2HO_2a$ is shown black, that for 2OHa is given in red.

As shown in Figure 3.12, the free energies for activation of •OH attacks are about 18 kcal·mol^{-1} lower than those of HO_2 attack. This outcome can be explained by resonance stability of the radicals: the peroxy radical can resonate the radical between two oxygen atoms whereas hydroxyl radical cannot conduct such resonance stability. Furthermore, the attack of HO_2• to BE-1T is endothermic whereas OH radical attacks are exothermic. In terms of free energy, BE-1T(C)-OH adduct is about 31 kcal·mol^{-1} more stable than BE-1T(C)-OOH adduct. Interestingly, throughout the rest of the free energy diagram of the reactions $2HO_2$a and 2OH, approximately 31-32 kcal·mol^{-1} free energy difference is maintained. Since the hydrogen of hydroxyl group in BE-1T(C)-OH adduct is in close contact the π-electrons of the thiophene ring, the polar hydrogen-π interaction stabilizes this product. However, BE-1T(C)-OOH does not have such an interaction to stabilize itself. The first step where O_2 attacks the carbon is kinetically very favorable: free energies of activation and reaction of the stepwise mechanisms (2OHa and $2HO_2$a) are around 14 kcal·mol^{-1}, however the product has lower stability. The free energy of reaction of 2OHb and $2HO_2$b are 9.4 kcal·mol^{-1}and 11.5 kcal·mol^{-1}. The second step, where the oxygen attacks the sulfur and breaks the bond, is kinetically less favorable with free activation energies around 26 kcal·mol^{-1} but thermodynamically much more favorable with free energies of reaction around 84 kcal·mol^{-1}.

The concerted $^3O_2$ addition reactions (2OHb and $2HO_2$b), of $^3O_2$ to BE-1T(C)-OH and BE-1T(C)-OOH adducts following the doublet manifold have extremely high free energies of activation of 61.3 kcal·mol^{-1} and 61.6 kcal·mol^{-1}, respectively (Figure 3.13.). The product has a four membered ring, which is composed of a carbon, two oxygens, a sulfur, causing a ring strain. Therefore, the free energy of reaction are very high for 2OHb and $2HO_2$b as well (55.5 kcal·mol^{-1} and 54.4 kcal·mol^{-1}).

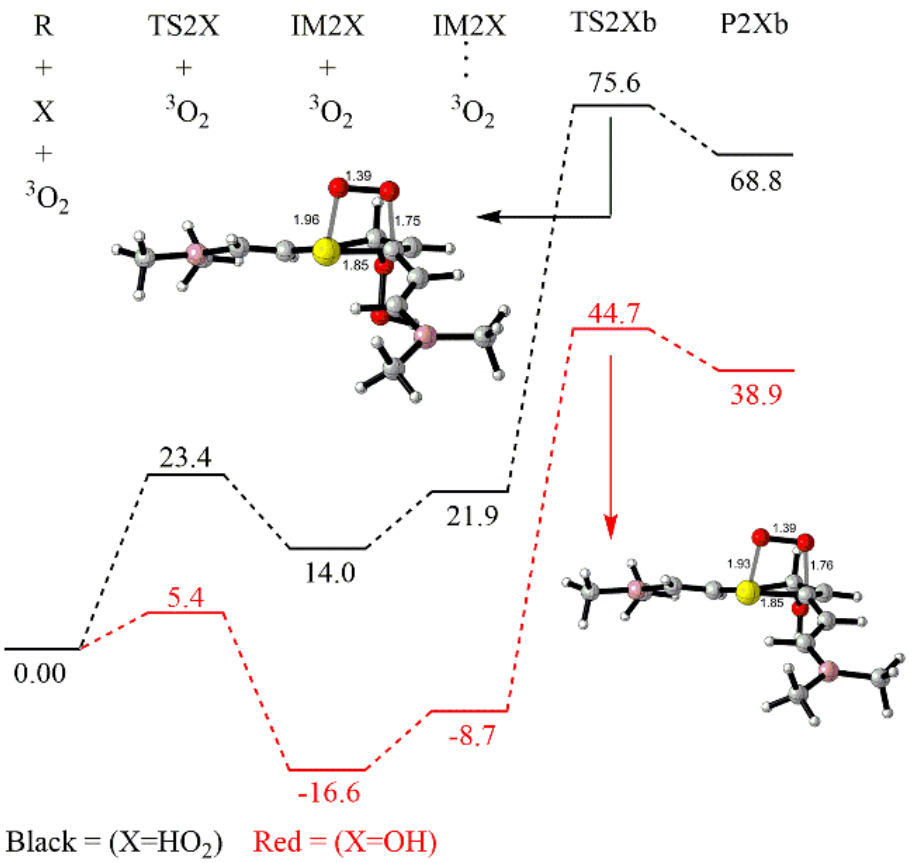

Figure 3.13. Free energy profile (kcal·mol^{-1}) for Mechanisms 2HO$_2$b (black), 2OHb (red) for BE-1T.

To understand the importance of boron in the stability of the molecule, dimethylboryl groups in BE-1T are replaced with hydrogen atoms to yield E-1T (2,5- bis(ethenyl)thiophene). The absence of boron affects neither the thermodynamic nor the kinetic stability of the initial radical reactions studied under this section. Furthermore, the absence of three-coordinate boron prohibits the location of a concerted O_2 attack. Even though the absence of boron, wipes out the possibility of degradation through the concerted mechanism, it facilitates its degradation along the stepwise mechanism. For BE-1T, the degradation via a concerted mechanism is almost impossible to occur due to thermodynamic and kinetic reasons, thus three-coordinate boron renders this set of oligothiophenes less prone to oxidative degradation.

Table 3.2. Gibbs energies of activation ($\Delta G^{\neq}$) for Mechanisms 2OHa, 2OHb and $2HO_2$a, $2HO_2$b (B3LYP/6-31G(d) for H, B, C, O and 6-311++G(3df,3pd) for S).

	BMBE-1T	BE-1T	E-1T	1T	BE-1T	BE-2T	BE-3T
2OH		5.4			5.4		
$2OHa_1$		-2.3	-4.1		-2.3		
$2OHa_2$		19.0	17.1		19.0		
2OHb		44.7			44.7		
$2HO_2$	22.9	23.4	23.0	27.0	23.4	23.3	21.9
$2HO_2a_1$	27.9	28.7	26.7		28.7	28.4	27.0
$2HO_2a_2$	49.9	51.9	48.6	41.7	51.9	50.5	46.9
$2HO_2$b		75.6			75.6		

$\langle S^2 \rangle$ is the total spin squared operator. $\langle S^2 \rangle$ equals to S(S+1) and S should be 0.5 for doublet and 1.5 for quartet. From Figure 3.14 up to Figure 3.22 the $\langle S^2 \rangle$ values are listed. Since our calculations are conducted in doublet energy level, $\langle S^2 \rangle$ value should be around 0.75 to rule out spin contamination. For the quartet energy level this value should close to 3.75. As observed in the aforementioned figures, these values are around 0.75 except for the pre-reactive complexes IM2Xa...O_2 for BE-1T, BE-2T, BE-3T, BMBE-1T. Since these values do not concern the calculated free energy barriers, they do not constitute any problem [46].

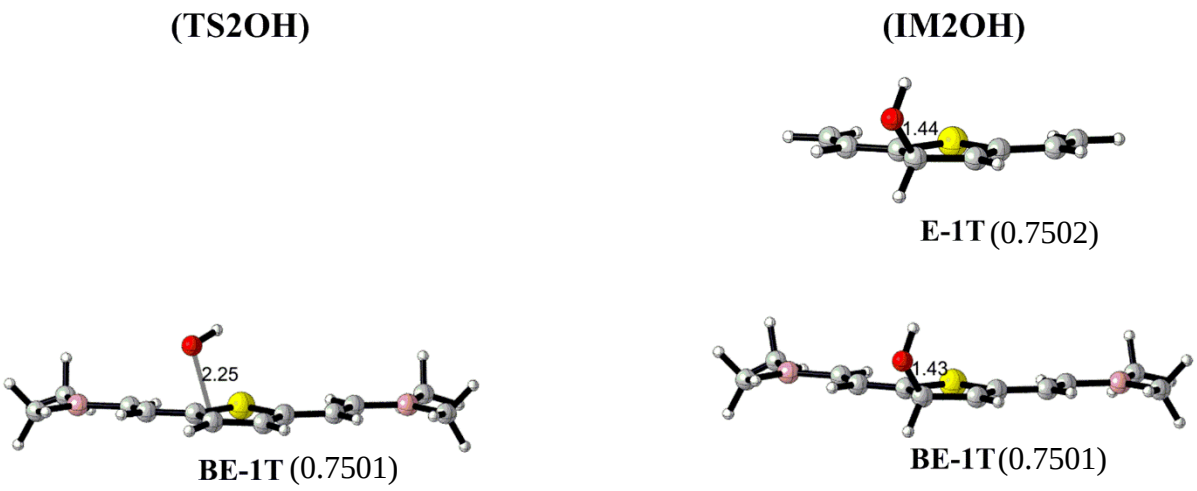

Figure 3.14. Optimized structures of TS2OH, and IM2OH (B3LYP/6-31G(d) for H, C, N, O and 6-311++G(3df,3pd) for S in vacuum).

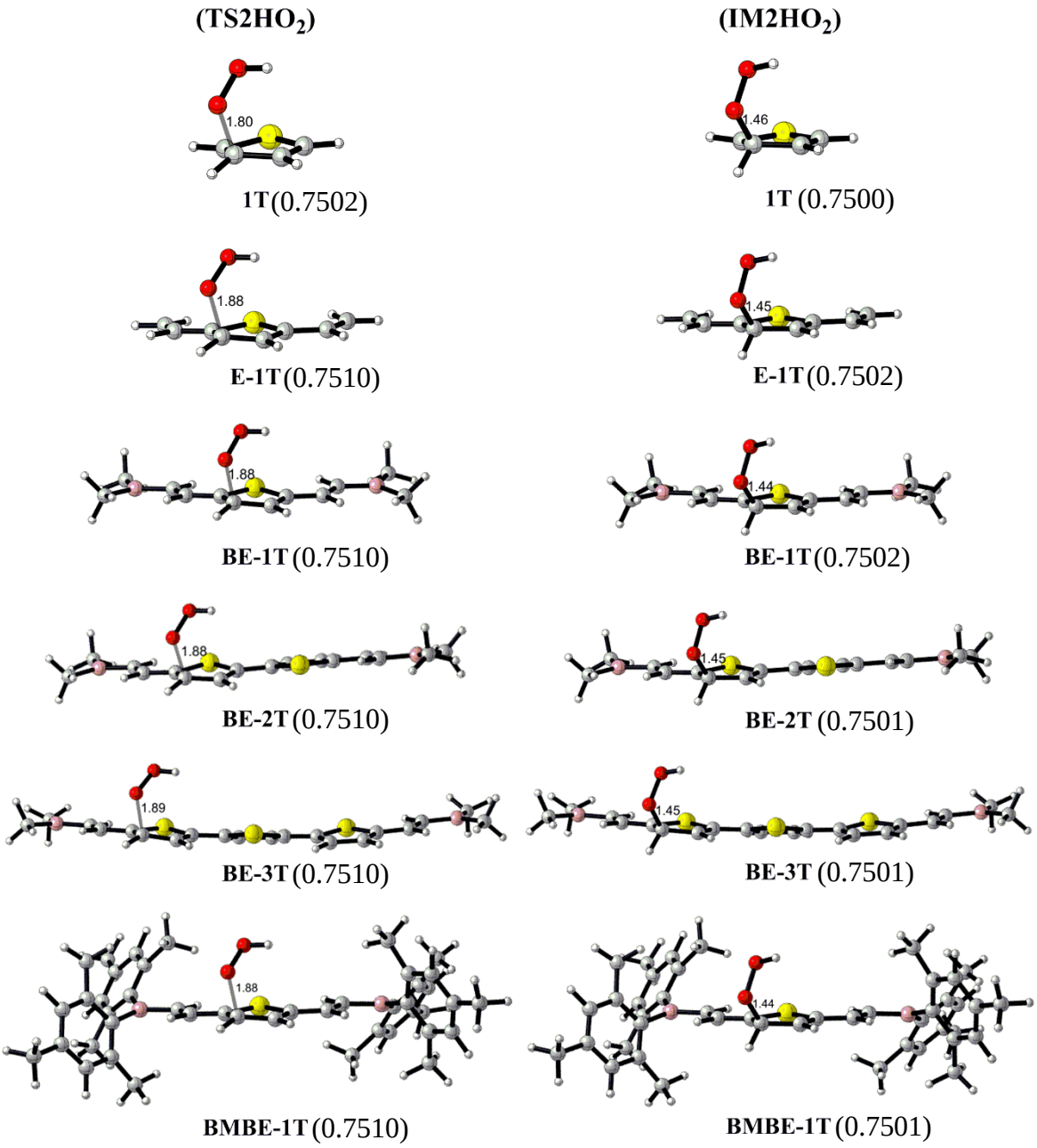

Figure 3.15. Optimized structures of $TS2HO_2$, and $IM2HO_2$ (B3LYP/6-31G(d) for H, C, N, O and 6-311++G(3df,3pd) for S in vacuum).

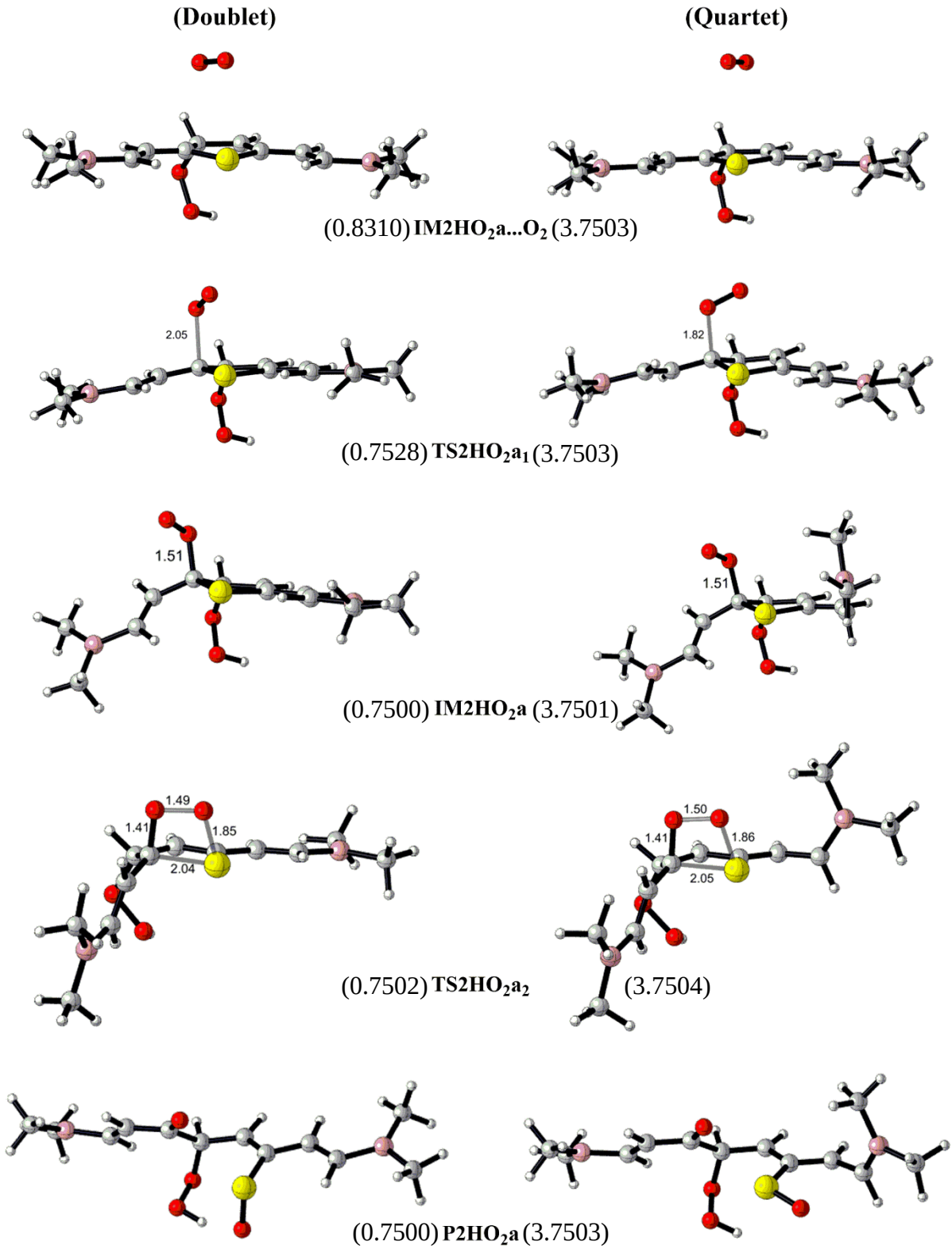

Figure 3.16. Optimized structures of IM2HO$_2$a...O$_2$, TS2HO$_2$a$_1$, IM2HO$_2$a, TS2HO$_2$a$_2$, and P2HO$_2$a for BE-1T at doublet and quartet energy state (B3LYP/6-31G(d) for H, C, N, O and 6-311++G(3df,3pd) for S in vacuum).

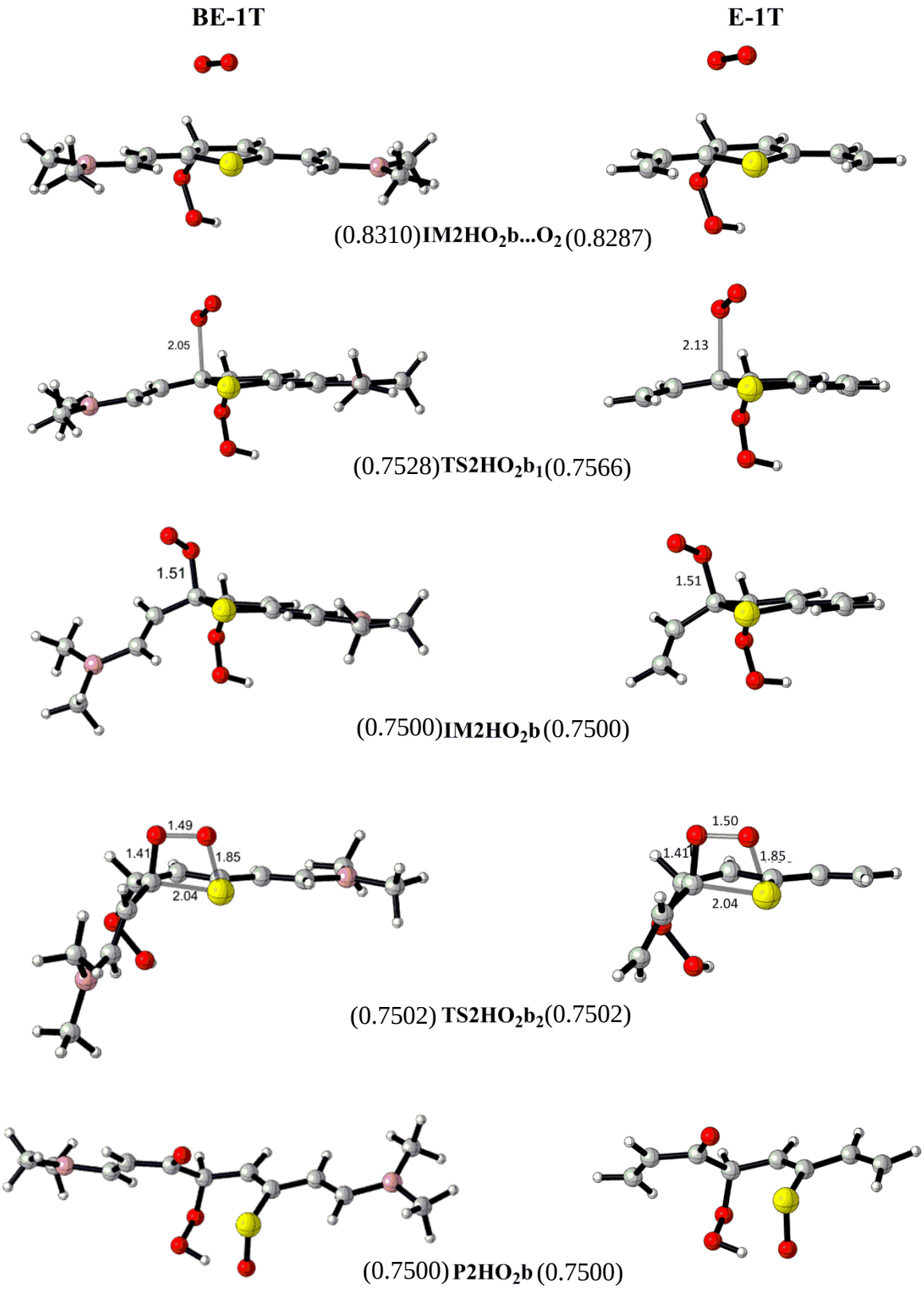

Figure 3.17. Optimized structures of IM2HO$_2$a...O$_2$, TS2HO$_2$a$_1$, IM2HO$_2$a, TS2HO$_2$a$_2$, and P2HO$_2$a for BE-1T and E-1T (B3LYP/6-31G(d) for H, C, N, O and 6-311++G(3df,3pd) for S in vacuum).

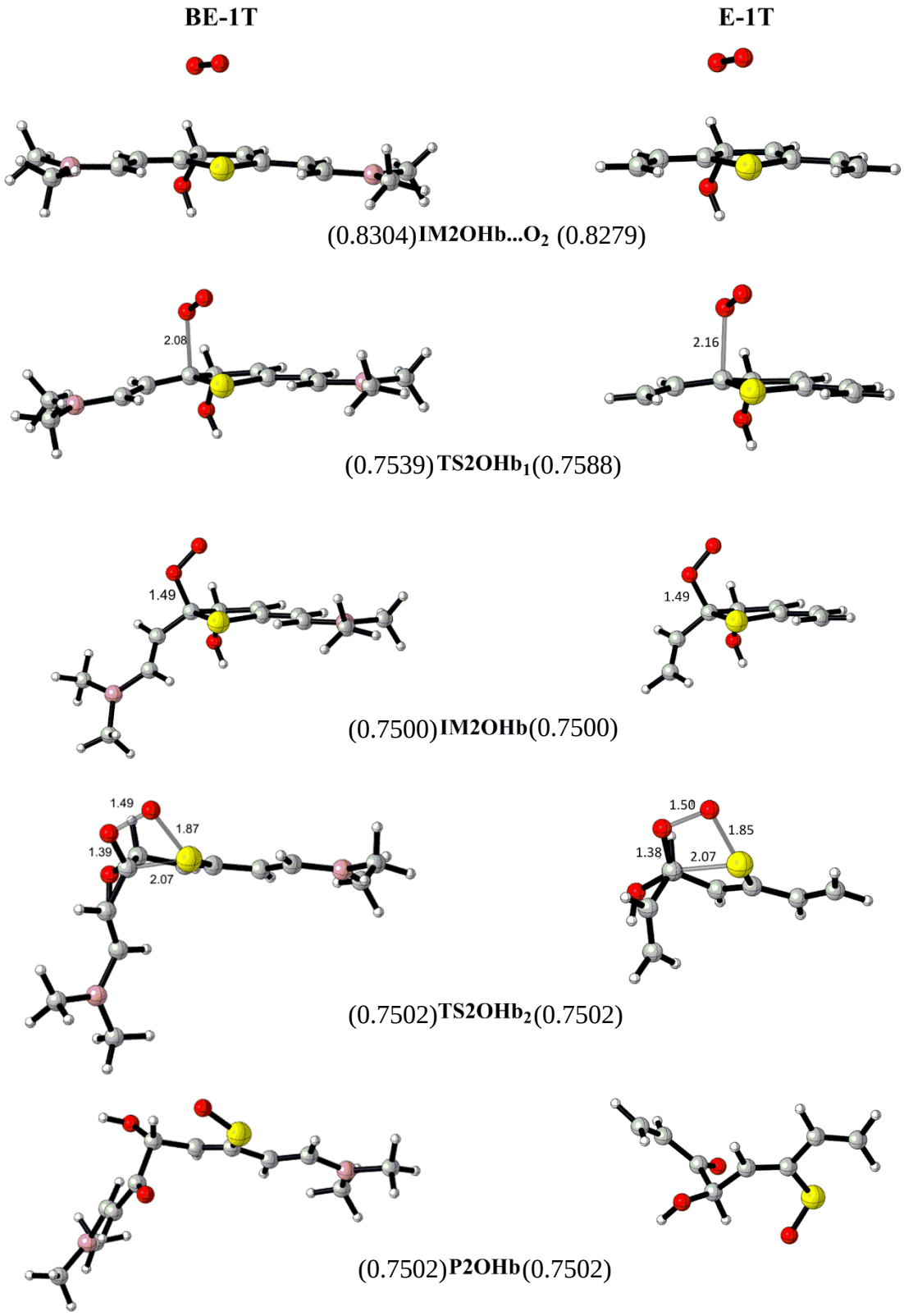

Figure 3.18. Optimized structures of IM2OHa...O_2, TS2OHa$_1$, IM2OHa, TS2OHa$_2$, and P2OHa for BE-1T and E-1T (B3LYP/6-31G(d) for H, C, N, O and 6-311++G(3df,3pd) for S in vacuum).

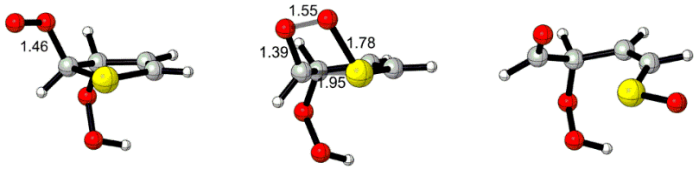

IM2HO$_2$a (0.7500) **TS2HO$_2$a$_2$** (0.7501) **P2HO$_2$a** (0.7501)

Figure 3.19. Optimized structures of IM2HO$_2$a, TS2HO$_2$a$_2$, and P2HO$_2$a for 1T (B3LYP/6-31G(d) for H, C, N, O and 6-311++G(3df,3pd) for S in vacuum).

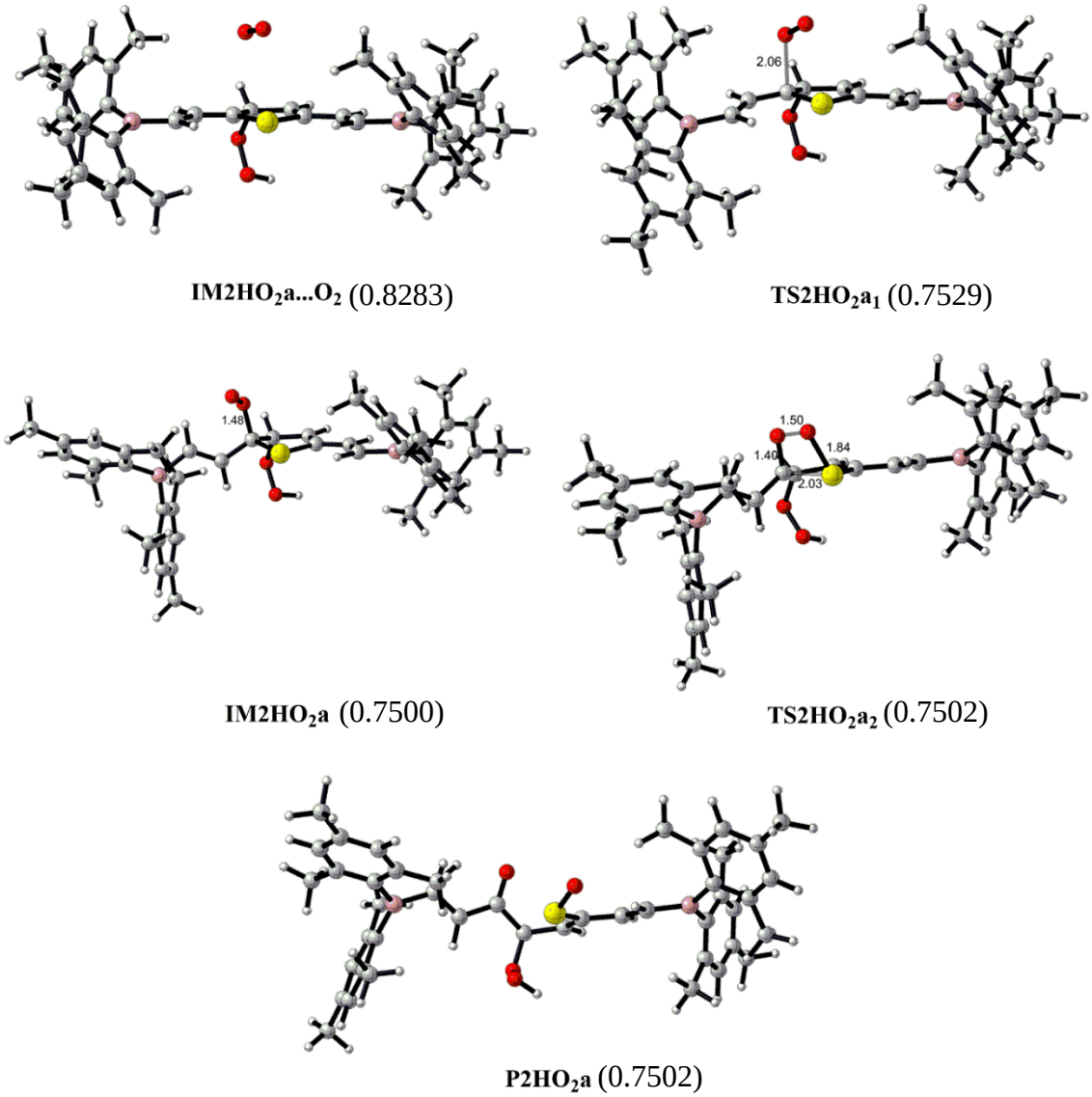

IM2HO$_2$a...O$_2$ (0.8283) **TS2HO$_2$a$_1$** (0.7529)

IM2HO$_2$a (0.7500) **TS2HO$_2$a$_2$** (0.7502)

P2HO$_2$a (0.7502)

Figure 3.20. Optimized structures of IM2HO$_2$a...O$_2$, TS2HO$_2$a$_1$, IM2HO$_2$a, TS2HO$_2$a$_2$, and P2HO$_2$a for BMBE-1T (B3LYP/6-31G(d) for H, C, N, O and 6-311++G(3df,3pd) for S in vacuum).

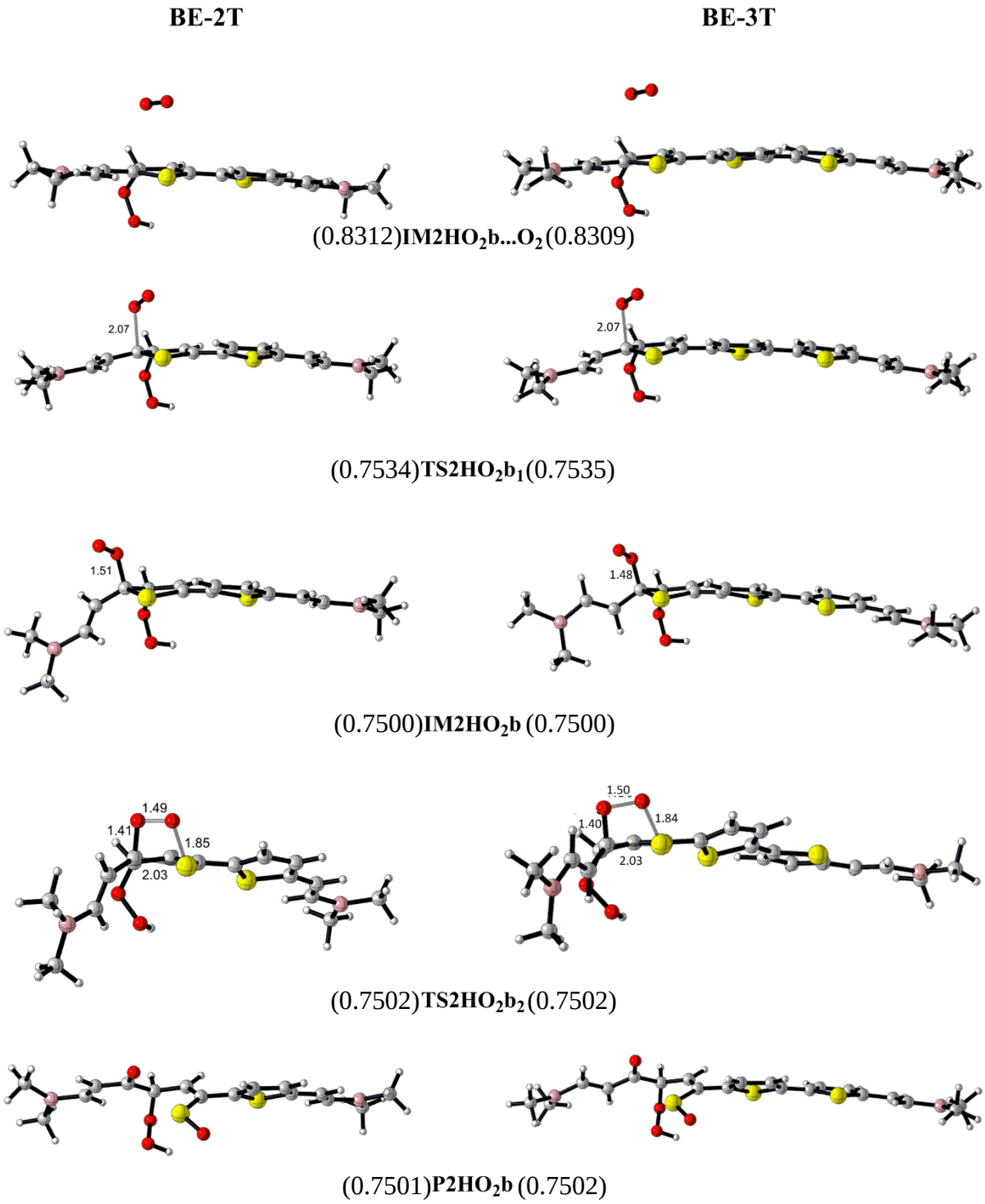

Figure 3.21. Optimized structures of IM2HO$_2$a...O$_2$, TS2HO$_2$a$_1$, IM2HO$_2$a, TS2HO$_2$a$_2$, and P2HO$_2$a for BE-2T and BE-3T (B3LYP/6-31G(d) for H, C, N, O and 6-311++G(3df,3pd) for S in vacuum).

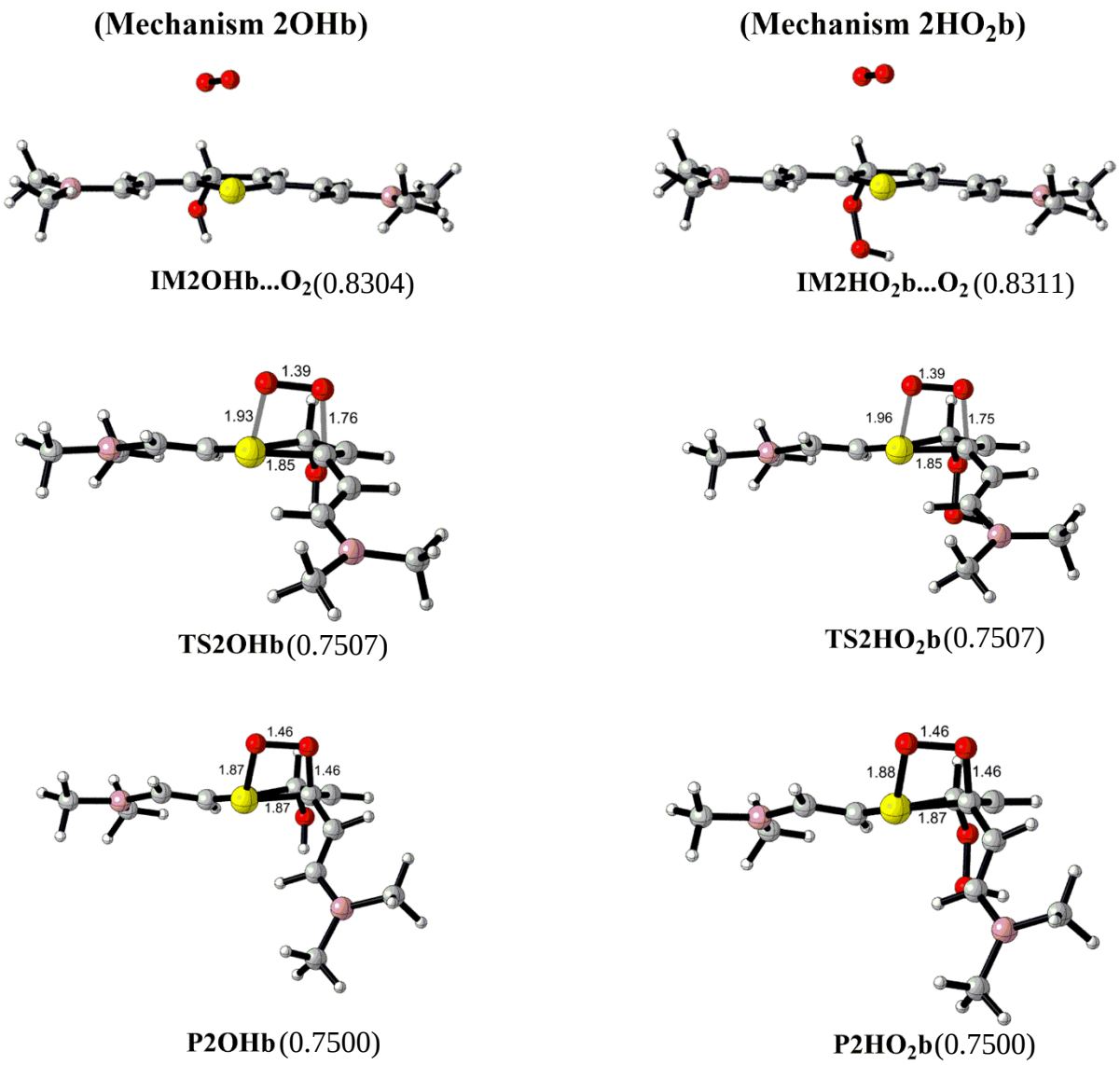

Figure 3.22. Optimized structures of IM2OHa...O_2, TS2OHb, P2OHb, IM2HO_2b...O_2, TS2HO_2b, P2HO_2b for BE-1T (B3LYP/6-31G(d) for H, C, N, O and 6-311++G(3df,3pd) for S in vacuum).

3.3.3. Mechanisms 3a, 3b and 3c: Concerted $^1O_2$ Addition Pathways

Singlet molecular oxygen ($^1O_2$) is generated via photoactive materials through photosensitization, where triplet ground state molecular oxygen is excited to its lowest excited singlet state. It is more reactive than triplet molecular oxygen ($^3O_2$) due to its higher energy, thus the degradation via a singlet molecular oxygen is expected to be kinetically more favorable.

Accordingly, we have modeled the degradation mechanism based on the singlet molecular oxygen addition to this set of oligothiophenes. The reactions investigated in this section have been selected based on the study of Song et al. on the degradation of thiophene [40]. The stepwise singlet molecular oxygen attacks on two different atoms on thiophene ring or the neighbouring hydrogens have been modeled. Those two atoms are carbons in positions C_β and $H_{ethylene}$ (Mechanism 3a), C_α and S (Mechanism 3b), both carbons in α positions (Mechanism 3c). Energy of the lowest excited singlet state of molecular oxygen is calculated by adding the empirical energy gap corresponding to the singlet-triplet energy gap (22.5 kcal·mol^{-}1) to the triplet state energy of molecular oxygen [47]. Since S value is 0 for singlet energy level, $\langle S^2 \rangle$ value should be 0 to rule out spin contamination. To see if there is spin contamination in our results, $\langle S^2 \rangle$ values are checked and confirmed to be 0 except for TS3b$_1$ and IM3b. Hence, structures seen in Figure 3.28 of TS3b$_1$ and IM3b are spin contaminated, which lowers the free energy due to the contamination by low lying high spin, triplet molecular oxygen (Figure 3.27).

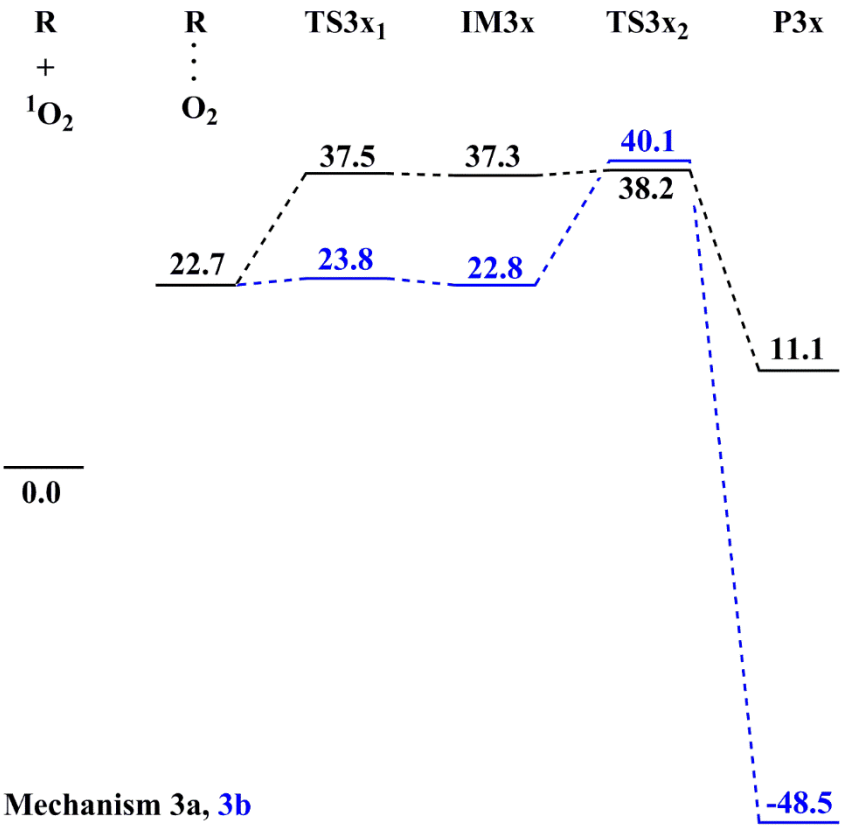

Figure 3.23. Potential energy surface diagram (kcal·mol^{-1}) for **BE-1T** for Mechanism 3a (black), 3b (blue).

As already demonstrated in section 4.3.1. and 4.3.2., BE-1T, BE-2T and BE-3T can be considered models for the degradation of BMBE-1T, BMBE-2T and BMBE-3T. As the number of thiophenes increases, neither the free energy of reaction of 3a nor the free energy barrier of 3a show critical changes (Figure 3.24.). Furthermore the distances shown in Figure 3.25 and Figure 3.26. are same for BE-1T, BE-2T and BE-3T. Hence, BE-1T is chosen as a model for the reactions that follow.

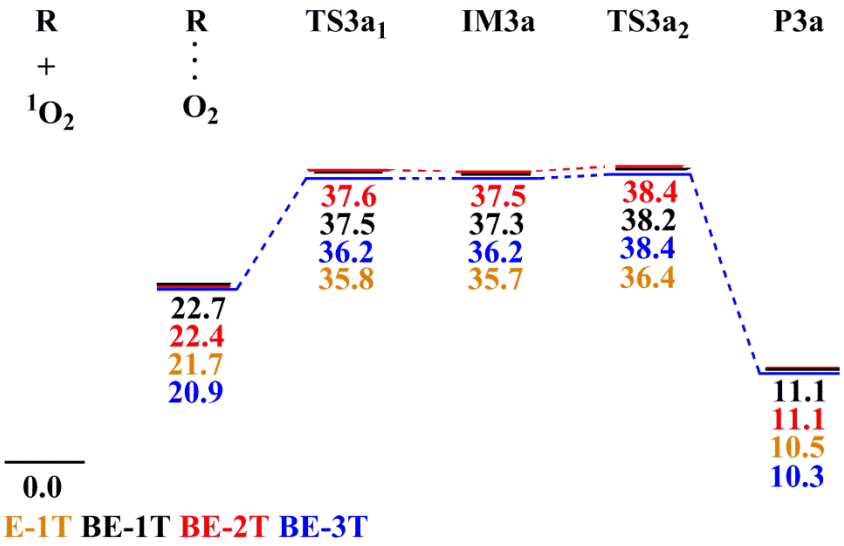

Figure 3.24. Free energy profile (kcal·mol^{-1}) for Mechanism 3a for E-1T, BE-1T, BE-2T and BE-3T.

In Figure 3.25. the first step of the Mechanism 3a, singlet molecular oxygen attack on C_β, is kinetically and thermodynamically very unfavorable however the second step where H abstraction from the ethylene group proceeds, kinetic demand is low, roughly 1 kcal·mol^{-1} and the resulting product is 10 kcal·mol^{-1} more stable than the pre-reactive complex formed between reactant and O_2. As mentioned before, the first step of Mechanism 3b, singlet molecular oxygen attack on C_α, is contaminated by the high spin low energy triplet molecular oxygen. For further analysis, this can be corrected using Yamaguchi's approximate spin projection method [46]. For the analysis of Mechanism 3c, 1,4-cycloaddition, Density Functional Theory (DFT) may nnot be

adequate, thus cannot be enough. Thus Complete Active Space Self-Consistent Field (CASSCF) will be used. This part is also left as a future work to be done by CASSCF.

To learn about boron's effect on these reactions, BE-1T is compared with E-1T where dimethylboryl groups are substituted with H atoms. Even if global trends are difficult to generalize the presence of boron seems to slightly lower the activation free energy in Mechanisms **3a** by roughly 2 kcal·mol^{-1}.

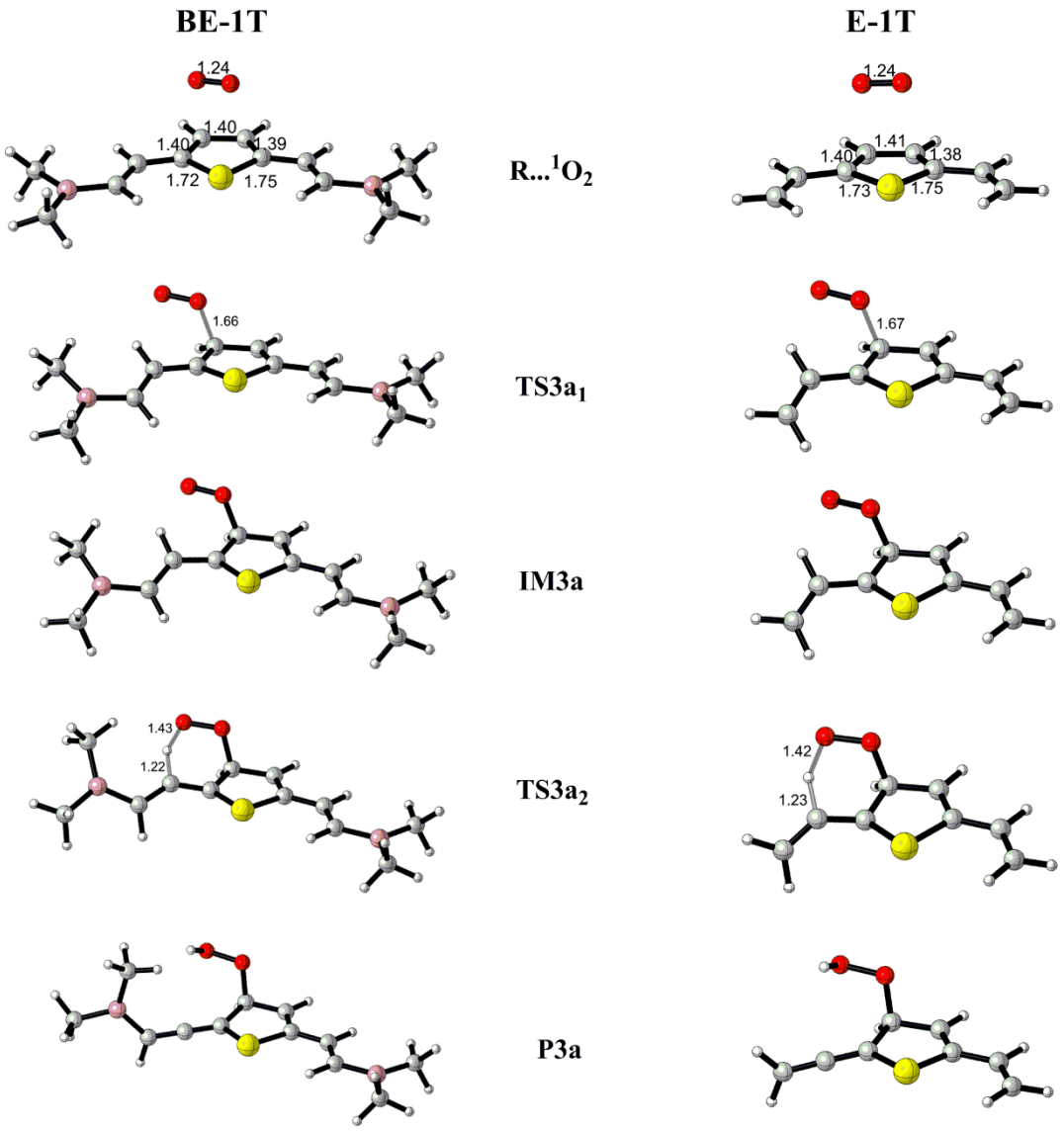

Figure 3.25. Optimized structures of R...$^1O_2$, TS3a$_1$, IM3a, TS3a$_2$, P3a for BE-1T and E-1T (B3LYP/6-31G(d) for H, C, N, O and 6-311++G(3df,3pd) for S in vacuum).

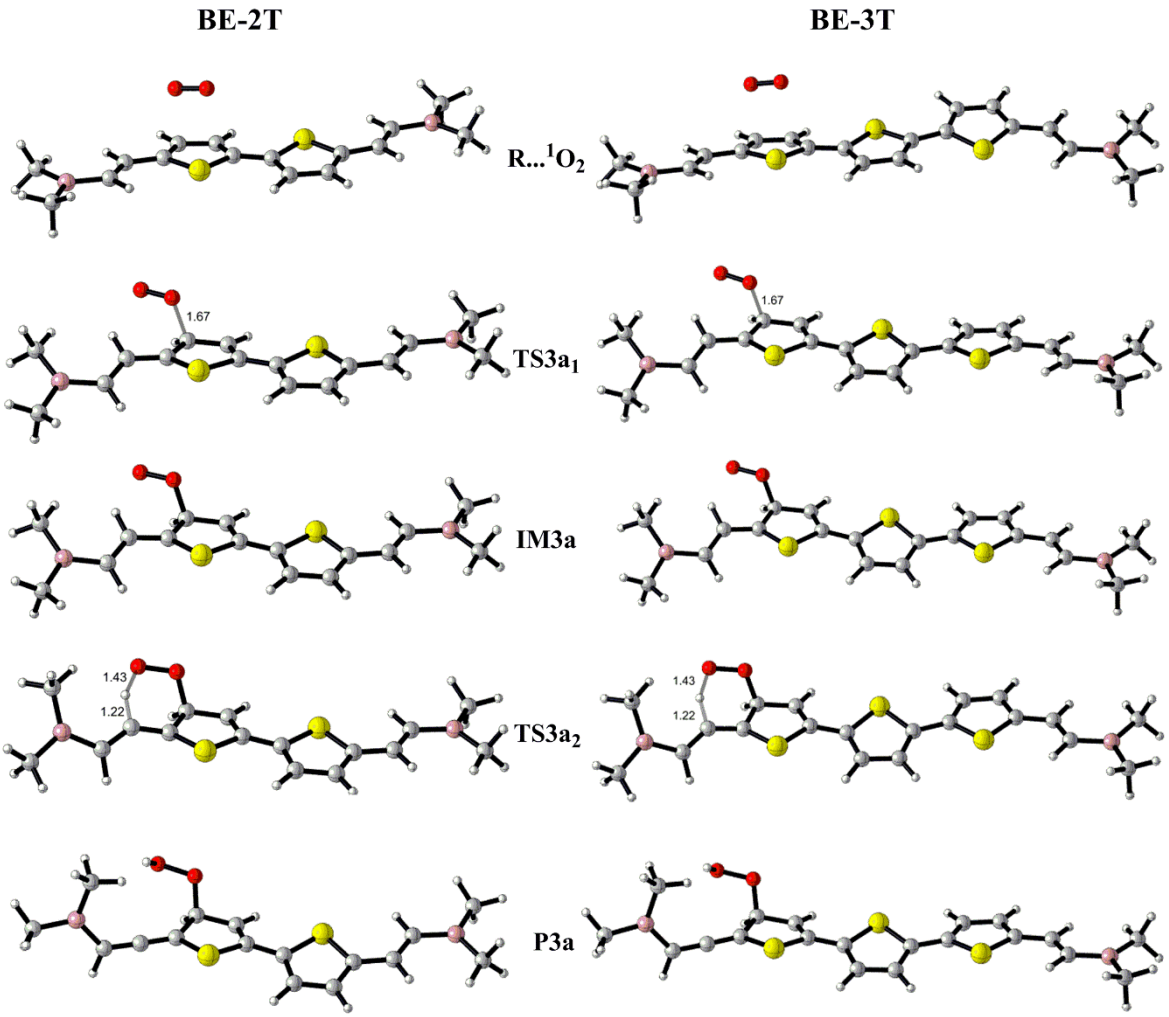

Figure 3.26. Optimized structures of R...$^1O_2$, TS3a$_1$, IM3a, TS3a$_2$, P3a for BE-2T and BE-3T (B3LYP/6-31G(d) for H, C, N, O and 6-311++G(3df,3pd) for S in vacuum).

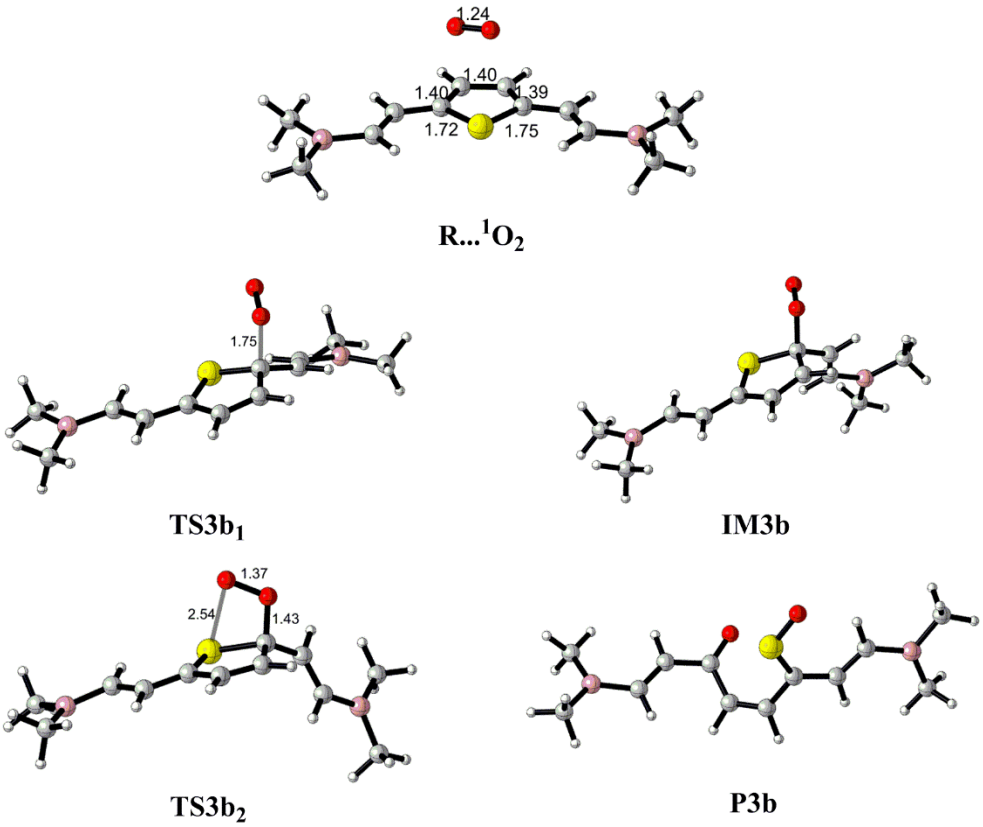

Figure 3.27. Optimized structures of R...$^1O_2$, TS3b$_1$, IM3b, TS3b$_2$, P3b for BE-1T (B3LYP/6-31G(d) for H, C, N, O and 6-311++G(3df,3pd) for S in vacuum).

3.4. Conclusion

A quantum mechanistic study of the possible oxidative degradation pathways for the selected boron containing oligothiophenes has been carried out at B3LYP/6-31G(d) level of theory using the geometries at the same level.The extra basis set (6-311++G(3df,3pd)) is used for the sulfur atom. Reaction pathways have been examined under three topics, namely, sulfoxide formation, sequential addition, and concerted $^1O_2$ addition. For Mechanisms 1 and 2HO$_2$b, BMBE-1T shows similar degradation trends as BE-1T, BE-2T, and BE-3T; the number of thiophene rings does not affect the degradation trend. As a consequence, BE-1T can be used safely to understand the aforementioned photo-oxidative degradation mechanisms.

In Mechanism 1, for BE-1T reaction 1_2 has the lowest free energy barrier (7.7 kcal·mol^{-1}). SOH adduct is very thermodynamically unstable, the energy barrier to reach a much thermodynamically stable S=O adduct is very low. Thus, formation of S=O adduct is the main degradation route also for these set of oligothiophenes. As the number of thiophenes increases, the free energy barrier does not change much but the reaction free energy increases. For reaction 1_2, E-1T has a free energy barrier of 9.9 whereas BE-1T has free energy barrier of 7.7 kcal·mol^{-1}. Hence incorporation of three-coordinate boron results in slightly lower stability in this case.

Among Mechanisms 2Xa and 2Xb, 2OHa demonstrates the lowest energy barriers. Attack of hydroxyl radical is more favorable than attack of hydroperoxyl radical kinetically and thermodynamically. For BE-1T in reactions 2OH and 2HO_2, free energy barriers are 5.4 kcal·mol^{-1} and 23.4 kcal·mol^{-1}, while free reaction energies are -16.6 kcal·mol^{-1} and 14.0 kcal·mol^{-1}. Free barrier energies for the first and second step of stepwise $^3O_2$ addition reactions (2OHa_1 and 2OHa_2) are 14.3 kcal·mol^{-1} and 26.2 kcal·mol^{-1}. The first step is kinetically favored but thermodynamically unfavored. For the second step the situation is the opposite. E-1T shows quite close barriers: free energy barriers for 2OH, 2OHa1 and 2OHa2 are 6.1 kcal·mol^{-1}, 12.5 kcal·mol^{-1} and 26.8 kcal·mol^{-1}.

In Mechanisms 3a, 3b and 3c, singlet molecular oxygen attacks are considered. Only the modelling of Mechanisms 3a is done completely. The addition of singlet molecular oxygen to C_β is kinetically and thermodynamically unfavorable, but the H abstraction from the ethylene kinetically demands roughly 1 kcal·mol^{-1} more energy and the product is thermodynamically more stable than the pre-reactive complex. Potential free energy surface of Mechanism 3a for E-1T lies 1-2 kcal·mol^{-1} below than that for BE-1T, pointing out that E-1T could be degrading slightly more easily.

4. THE IGNITION REACTIONS OF HYPERGOLIC PROPELLANTS

4.1. Introduction

Hypergolic propellants are vastly used in astronautics for space propulsion. In the rocket engine, fuel and oxidizer components ignite spontaneously upon mixing. Therefore, having no need for an ignition system enables it to fire repeatedly by simply opening and closing the valves of the propellant. In addition both fuel and oxidizer components of the hypergolic propellant can be stored at room temperature. Hydrazine (N_2H_4) and various hydrazine derivatives, such as monomethylhydrazine (MMH) and unsymmetrical dimethyl hydrazine (UDMH), were commonly used as hypergolic fuels in the past [46–48]. However, due to environmental and human health concerns, fuel liquids with lower toxicity and no carcinogenicity are scrutinized. Tertiary alkyl multiamines and amine azides were considered less toxic and noncarcinogenic candidates to replace hydrazine and its derivatives. N, N, N', N'-tetramethylethylenediamine (TMEDA) is a tertiary alkyl multiamine with compatible ignition delay time with hydrazine whereas, 2-azido-N,N-dimethylethan-1-amine (DMAZ) is an amine azide with a less desirable (higher) ignition delay time. White fuming nitric acid (WFNA) and red fuming nitric acid (RFNA) are common oxidizers used in the hypergolic propellants. They both are highly corrosive. Stevenson has claimed the synergic effect to occur when TMEDA and DMAZ are used as a mixture [51]. Bittner *et al.* have studied this phenomenon to show that TMEDA/WFNA, and DMAZ/WFNA mixtures yield an ignition delay time of 17 ms and 96 ms in the given order, on the other hand 30% DMAZ to 70% TMEDA/WFNA has a lower ignition delay time (11ms) than TMEDA/WFNA [7].

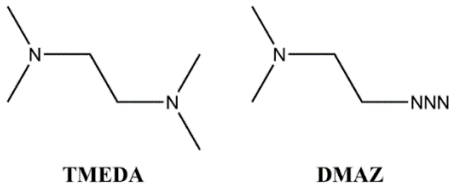

Figure 4.1. Structures of TMEDA and DMAZ

Ignition mechanisms of TMEDA and DMAZ have been investigated separately through experiments and computations. Wang *et al.* have initially observed salt formation during the drop test of TMEDA, this is claimed to play an important role in the preignition reaction between TMEDA and nitric acid both in the condensed phase and the gas phase. The authors have concluded that reactions were initiated upon the exothermic formation of a salt which consists of trialkylammonium and nitrate anion. In the gas phase, the vapors of the ion pair condenses to a solid particulate cloud at low temperatures and start to decompose rapidly. In the condensed phase, the exothermicity of the reaction by salt formation facilitates the decomposition of HNO_3 into NO_2, O_2, and H_2O. Among the aforementioned oxidative species, NO_2 would be responsible for H radical abstraction and recombination reactions with radicals formed from TMEDA [52]. Liu et al. have modeled the salt formation and ignition reactions of various multiamines with NO_2 to correlate the exothermicity of salt formation and reaction rates to the ignition delay time. The reactions they have suggested start with the H-abstraction reactions by NO_2, NO_2 coupling reactions with the radical derivatives of TMEDA and β scission reactions of the NO_2 coupled species [53]. Zhang et al. have also used H-abstraction, NO_2 coupling and β scission reactions to discuss the ignition delay time difference between the fuels, TMEDA and DMAZ. They correlated the low H abstraction barrier of TMEDA by NO_2 to its ignition delay time. Furthermore they have concluded that the number of amino groups in TMEDA and DMAZ would be responsible for the ignition delay time differences between these two fuels because proton transfer from nitric acid to nitrogen atoms of the amine groups is assumed to be the most important exothermic initiation step [54]. Labbe has studied the pre-ignition reactions of TMEDA/RFNA in a theoretical framework and suggested a potential degradation mechanism as seen in Figure 4.2. [55]. In this diagram, pre-ignition reactions start via H radical abstraction, a series of homolytic cleavage reactions subsequently take place rather than recombination with NO_2. Needham [56] monitored TMEDA/HNO_3 ignition at 2000K employing ReaxFF, a bond order-based force field, in Reactive Molecular Dynamics (RMD) simulations. He points out that HNO_3 splits into •OH, and NO_2. Furthermore, •OH is considered as the major radical source for H abstraction because there is no •OH build up in the system and H_2O quickly becomes one of the major products. Chen et al. have assessed various spin-allowed and spin-forbidden paths for thermal degradation of DMAZ by optimizing the geometries at MPWB1K/6-31+G(d,p) and calculating the relative energies at QCISD(T)/6-31++G(2df,p) and QCISD(T)/6-31++G(3df,2p) levels. Their results show that

among the investigated thermal decomposition reactions of DMAZ, N−N_2 bond fission, and formation for nitrene have the lowest barriers [57].

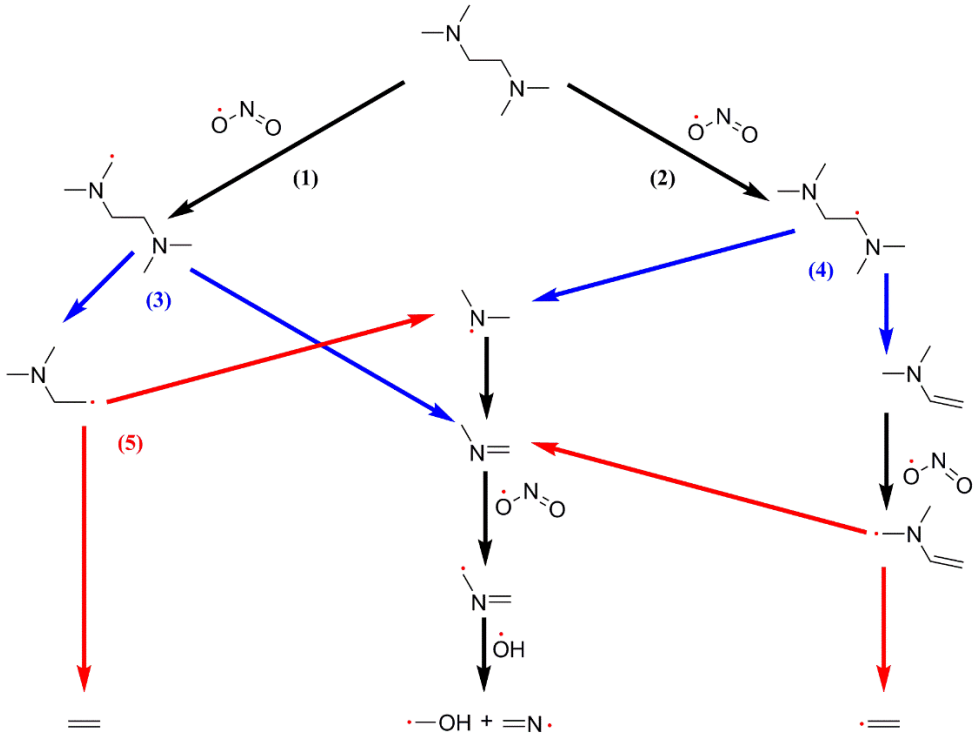

Figure 4.2. Major reaction route for stoichiometric TMEDA/RFNA combustion at P = 1 atm proposed by Labbe [55].

At this stage two factors seem to be responsible for the ignition of hypergolic propellants: the exothermicity of salt formation and the rates of pre-ignition reactions. Hence, in this study we would like to rationalize the ignition delay times of TMEDA/WFNA, DMAZ/WFNA, and TMEDA, DMAZ mixture/WFNA by exploring the reactions between the fuels (TMEDA, DMAZ) and nitric acid (NA).

4.2. Computational Methodology

The calculations are carried out with the Gaussian E09 software package [58] employing density functional theory (DFT). The Minnesota hybrid functional M06-2X with 54% HF, and the standard Pople basis set, 6-31++G(d,p), are used to carry out the calculations of the harmonic vibrational frequencies, the geometry optimizations of the ground state and transition state structures [56, 57]. Conformer search has been done around the single bonds for local minimum structures. The unrestricted approach is used for the open-shell species while the restricted

approach is used for the closed-shell species such as the salt formation. Ground state structures do not possess imaginary frequencies while transition state structures have a single imaginary frequency. Intrinsic reaction coordinate (IRC) calculations have been carried out for the transition state structures to justify the location of the transition state structures. Solvent parameters from pure nitric acid will be used for calculations regarding the salt formation. Polarizable Continuum Model (PCM) is employed to account for the effect of solvation. The dielectric constant of nitric acid ($\varepsilon_{\text{Pure Nitric Acid}} = 50$) and the solvent radius ($R_{\text{Pure Nitric Acid}} = 2.02$ Å) are taken from empirical data.

4.3. Results and Discussion

4.3.1. Salt Formation

Through a high-speed camera Wang *et al.* [52] recorded the formation of a white cloud where TMEDA and HNO_3 contacted each other. This result pointed out to a complexation between TMEDA and HNO_3: proton transfer from HNO_3 to the lone pairs of nitrogen atoms in TMEDA lead to the formation of TMEDA dinitrate salt. This phenomenon has been previously scrutinized computationally for TMEDA by Liu et al.[10] and for DMAZ by Chen et al. [61], but none of these publications has rationalized the ignition delay times of TMEDA, DMAZ and 2:1 TMEDA:DMAZ mixture by WFNA.

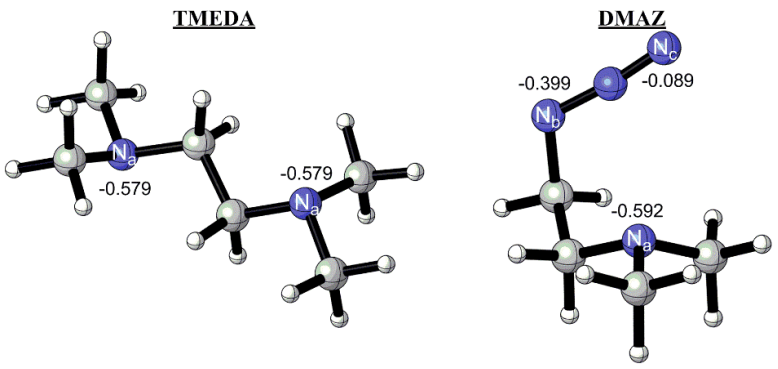

Figure 4.3. Equilibrium structures of TMEDA and DMAZ in solution. (M06-2X/6-31++G(d,p), ε = 50, R = 2.02 Å). NPA charges of the nitrogens are written next to each atom.

TMEDA being a tertiary amine has two long pair sites (N_a) which are equivalent to each other. On the other hand, DMAZ has three different long pair sites: the nitrogen of tertiary-amine (N_a), the azido nitrogen adjacent to the methylene group (N_b), and the terminal nitrogen of the azido group (N_c).

Table 4.1. Reaction energies (kcal·mol^{-1}) at 298.15K (M06-2X/6-31++G**)
(ε = 50, R = 2.02Å)

Reaction	**ΔE_{rxn}***	**ΔG_{rxn}**
TMEDA + HNO_3 ↔ TMEDA-(N_aH^+ NO_3^-)	-28.2	-16.9
TMEDA + 2 HNO_3 ↔ TMEDA-(N_aH^+ NO_3^-)$_2$	-53.1	-31.4
DMAZ + HNO_3 ↔ DMAZ-(N_aH^+ NO_3^-)	-25.4	-14.6
DMAZ + HNO_3 ↔ DMAZ-(N_b-HNO_3)	-10.0	0.1
DMAZ + HNO_3 ↔ DMAZ-(N_c-HNO_3)	-3.9	5.7
DMAZ + 2 HNO_3 ↔ DMAZ-(HNO_3)$_2$	-36.8	-13.3
DMAZ + 3 HNO_3 ↔ DMAZ-(HNO_3)$_3$	-38.5	-6.8

*Electronic and zero point energies are included.

Table 4.1. gathers the reaction energies of salt formation reactions in terms of electronic energies and free energies while Figure 4.4. shows the structures for the global minima of the HNO_3 complexes with TMEDA and DMAZ. Among the complexes displayed in Figure 4.4., N_a-H distances are always 1.06 Å whereas N_b-H distances range from 1.59 Å up to 1.69 Å as the number of HNO_3 molecules in the complex increases. The N_c-H distance also varies between 1.93 Å to 2.12 Å as HNO_3 molecules are added to the complex. These findings suggest that complexation between nitrogen atoms of azido group and HNO_3 display stronger interactions when they are considered individually. N_a carrying the most negative charge abstracts the proton from HNO_3 whereas N_b and N_c are at H-bond distance from HNO_3 The charge distribution on N atoms is responsible of the heats evolved during salt formation. The exothermicity for the formation of DMAZ-(N_aH^+ NO_3^-) is close to the value calculated for TMEDA-(N_aH^+ NO_3^-) but the complexation exothermicities of DMAZ-(N_b-HNO_3) and DMAZ-(N_c-HNO_3) are much smaller. Zhang et al. have previously calculated the HOMO energy level of the long pair sites in DMAZ to rationalize this

outcome. They found out that lone pair electrons of N_a occupy the highest occupied molecular orbital (HOMO) of DMAZ whereas electronic energies of the orbitals including the lone pairs of N_b and N_c are 44.9 and 137.4 kcal·mol^{-1} lower than that of the HOMO, rendering them interact less with the polar hydrogen of nitric acid [62]. The differences in the energetics of salt formation can also be explained by the NPA charges of the nitrogen atoms: nitrogen of the amine group (N_a) of DMAZ, has the largest local charge (-0.592), and nitrogen adjacent the alkyl group (N_b) has a smaller local charge (-0.399) and the terminal nitrogen of the azido group (N_c) has a much smaller local charge (-0.089). As NPA charges of nitrogen atoms decrease, the exothermicity of the reaction increases. In terms of free energy, considering complexation of HNO_3, with N_b formation is slightly endergonic and with N_c it is much more endergonic. Correspondingly, our calculations show that the formation free energy estimate of TMEDA-(N_aH^+ NO_3^-)$_2$ is 24.6 kcal·mol^{-1} lower than the calculated value for DMAZ-(HNO_3)$_3$. Addition of HNO_3 leads to ordered structures with an increase in entropy in every case: the larger the number of HNO_3 molecules added the more ordered the transition state is, the entropy decreases leading to slightly exergonic of endergonic reactions.

In summary, the energy is supplied by the formation of the TMEDA dinitrate salt and formation of DMAZ mononitrate salt's complexation with 2 HNO_3 groups. Results show that former species is 24.6 kcal·mol^{-1} more exothermic in terms of free energy. Salt formation exothermicity might be the weighty reason for the shorter ignition time of the fuel TMEDA.

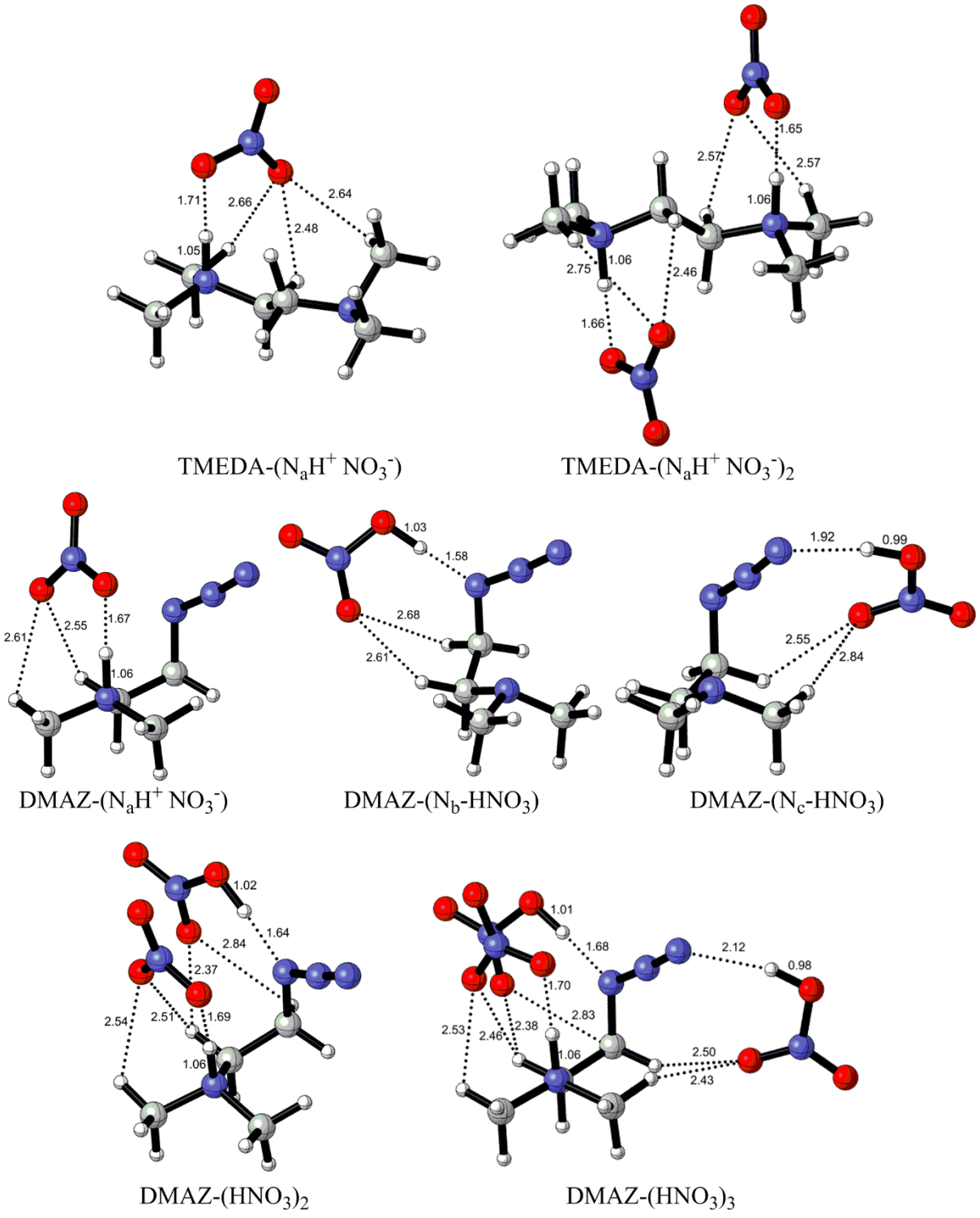

Figure 4.4. TMEDA-$(HNO_3)_x$ and DMAZ-$(HNO_3)_y$ complexes in solution. (M06-2X/6-31++G(d,p), ε= 50, R= 2.02 Å). Hydrogen bond distances (Å) are displayed.

4.3.2. Ignition Reactions

Through quantum mechanical calculations, Labbe [63] has proposed that ignition reactions of hypergolic propellant, TMEDA/IRFNA are initiated with H abstraction from the TMEDA. Later on Needham[17] has suggested that HNO_3 dissociates into •OH, and NO_2. Furthermore Needham states that H abstraction is carried out with •OH radical rather than NO_2. Hence, we decided to investigate this outcome for TMEDA and DMAZ separately. Thereafter, the mechanism proposed by Labbe [63] suggest β scission as the continuation of the ignition reactions of TMEDA/nitric acid pair. Accordingly, we adapted the ignition mechanism of TMEDA in Scheme 2 to DMAZ. Due to the azido group in DMAZ, $N{-}N_2$ bond fission, where formation of nitrene takes place, is also considered. Since TMEDA and DMAZ have boiling points of 121 and 135°C, we ran our calculations at 150°C (423K) in gas phase.

4.3.2.1. H-Abstraction by •OH/NO_2. Hydrogen abstraction reaction is assumed to be the initial step of the ignition reactions between TMEDA and IRFNA or nitric acid hypergolic bi-propellants according to experiments [52] and computational simulations [56]. The reactions considered in this section are given below.

For TMEDA:

R1:

$(CH_3)_2NCH_2CH_2N(CH_3)_2 + NO_2/{\bullet}OH \rightarrow {}^2(CH_2)(CH_3)NCH_2CH_2N(CH_3)_2 + HONO/H_2O$

R2:

$(CH_3)_2NCH_2CH_2N(CH_3)_2 + NO_2/{\bullet}OH \rightarrow (CH_3)_2N{}^2CHCH_2N(CH_3)_2 + HONO/H_2O$

For DMAZ:

R6:

$(CH_3)_2NCH_2CH_2NNN + NO_2/{\bullet}OH \rightarrow {}^2(CH_2)(CH_3)NCH_2CH_2NNN + HONO/H_2O$

R7:

$(CH_3)_2NCH_2CH_2NNN + NO_2/{\bullet}OH \rightarrow (CH_3)_2N{}^2CHCH_2NNN + HONO/H_2O$

R8:

$(CH_3)_2NCH_2CH_2NNN + NO_2/\bullet OH \rightarrow (CH_3)_2NCH_2{}^2CHNNN + HONO/H_2O$

H abstraction by NO_2 leads to *cis*-HONO, *trans*-HONO or HNO_2. As Liu[3] et al. have stated, our preliminary findings confirm that the formation of *cis*-HONO has the lowest barrier. Our discussion goes on by considering *cis*-HONO only. The hydrogens with the lowest charge are selected to be abstracted by a radical species. Both in TMEDA and DMAZ, the activation barrier for H abstraction with •OH is at least 10 kcal·mol^{-1} lower than the one for H abstraction by NO_2. Furthermore, formation of HONO is rather endothermic, whereas the formation of H_2O is exothermic. In Figure 4.5., C-H distances of the transition state (TS) structures of H abstraction by •OH are ~0.1 Å shorter than those in which NO_2 abstracts H. On the other hand, O---H distances in the transition structures with •OH are ~0.1-0.3 Å longer. Thus, the TS structures of the H abstraction by •OH resemble the reactants and the barriers are lower as compared to the abstraction by NO_2; this finding is in agreement with Hammond's postulate [64].

Table 4.2. Free energy profile (kcal·mol^{-1}) for H abstraction in TMEDA and DMAZ at 423°K (M06-2X/6-31++G(d,p).

Reaction	**$\Delta G^{\ddagger}$-NO_2(•OH)**	**ΔG_{rxn}-NO_2(•OH)**
R1	21.6 (9.0)	10.2 (-26.0)
R2	21.8 (6.1)	9.0 (-27.2)
R6	21.9 (9.1)	11.0 (-25.3)
R7	21.9 (8.2)	8.4 (-27.8)
R8	29.8 (10.6)	7.5 (-28.7)

Comparing TMEDA with DMAZ, in case of HONO formation R1-R6, R2-R7 pairs have free energy barriers around 21.6/21.9 kcal·mol^{-1}. R8 has a free energy barrier of 29.8 kcal·mol^{-1}. The main difference in the transition state structures of these reactions is that in R1-R6 and R2-R7 pairs, the free oxygen of the nitric acid makes hydrogen bonding with two hydrogen atoms but in R8 there is no such possibility of hydrogen bonding in the transition state structure. In the case of H abstraction by •OH, R1-OH and R6-OH have very close free energy barriers of 9.0 and 9.1 kcal·mol^{-1} whereas R2-OH and R8-OH have lower free energy barriers (6.1 and 8.2 kcal·mol^{-1} respectively) . This barrier difference between R2-OH and R7-OH can be ascribed

to the hydrogen bonding interaction between one of the nitrogen atoms of TMEDA and •OH further stabilizing TS2-OH (Figure 4.5.). R8-OH has free energy barrier of 10.6 kcal·mol^{-1}.

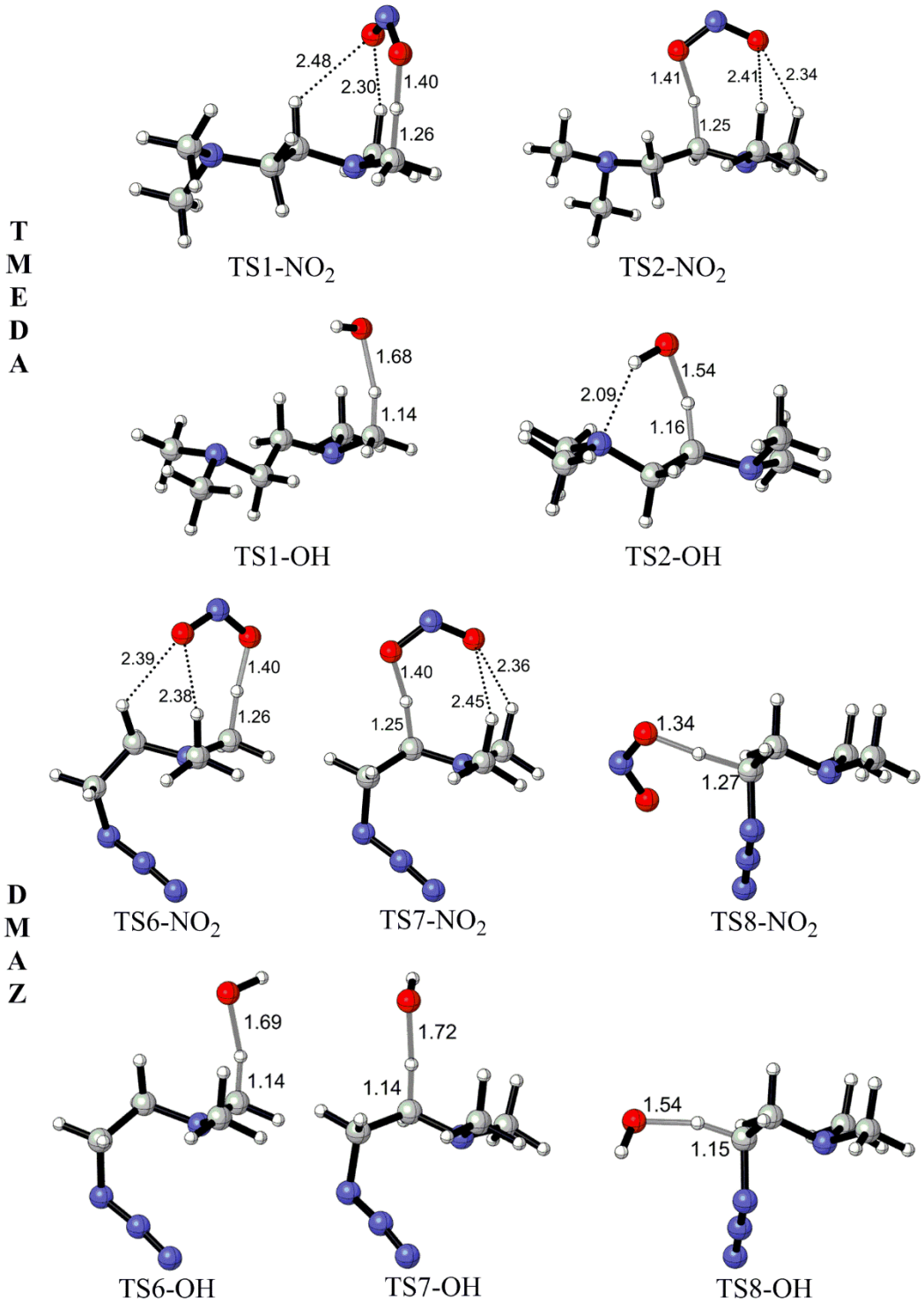

Figure 4.5. Transition state structures for H abstraction in TMEDA and DMAZ in vacuum (M06-2X/6-31++G(d,p). Bond distances are in Å.

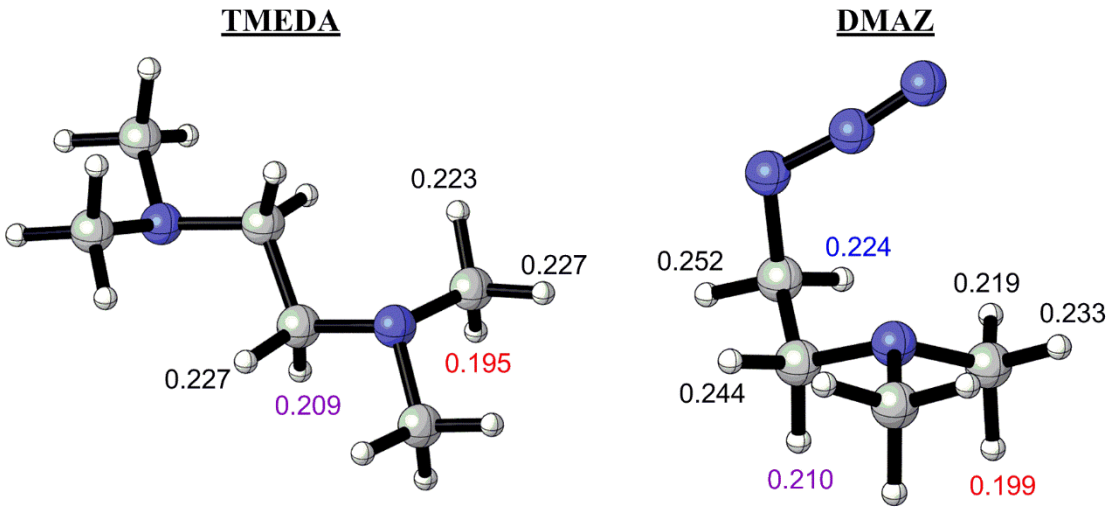

Figure 4.6. Equilibrium structures of TMEDA and DMAZ in vacuum . (M06-2X/6-31++G(d,p)) NPA charges of the nitrogens are written next to each atom.

In summary, the free reaction barriers for the H abstraction via •OH are much lower than those via NO_2. Thus, •OH could be the predominant species in the role of H abstraction. Considering H-abstraction, TMEDA and DMAZ show close free energies of activation.

4.3.2.2. β Scission Reactions. After the H abstraction, the proposed ignition mechanism of TMEDA focuses on the β scission reactions. Due to the radical nature of the reactant, a radical and a non-radical product are formed. As previously discussed, a carbon centered radical is formed. On the other hand, β scission can result in a nitrogen centered radical or a carbon centered radical, these are listed below.

For TMEDA:

R3: $^2(CH_2)(CH_3)NCH_2CH_2N(CH_3)_2 \rightarrow (CH_3)_2NCH_2{}^2CH_2 + CH_3N{=}CH_2$

R4: $(CH_3)_2N{}^2CHCH_2N(CH_3)_2 \rightarrow (CH_3)_2NCH{=}CH_2 + (CH_3)_2{}^2N$

R5: $(CH_3)_2NCH_2{}^2CH_2 \rightarrow C_2H_4 + (CH_3)_2{}^2N$

For DMAZ:

R9: $^2(CH_2)(CH_3)NCH_2CH_2NNN \rightarrow {}^2CH_2CH_2NNN + CH_3N{=}CH_2$

R10: $(CH_3)_2N^2CHCH_2NNN \rightarrow (CH_3)_2NCH=CH_2 + {}^2NNN$

R11: $(CH_3)_2NCH_2{}^2CHNNN \rightarrow (CH_3)_2{}^2N + NNNCH=CH_2$

R12: $NNNCH_2CH_2 \rightarrow C_2H_4 + {}^2NNN$

Table 4.3. Free energy profile (kcal·mol^{-1}) for β scission in TMEDA and DMAZ at 423°K (M06-2X/6-31++G(d,p))

Reaction	**$\Delta G^{\ddagger}$**	**ΔG_{rxn}**
R3	31.0	3.9
R4	24.5	-1.4
R5	24.6	-0.1
R9	29.9	5.9
R10	6.8	0.2
R11	26.4	3.7
R12	15.2	-2.9

Interestingly, these free energy barrier results are in agreement with the stability of the products. R3 and R9 both have free activation energies around 30 kcal·mol^{-1}, free reaction energies around 4-6 kcal·mol^{-1} and $CH_3N=CH_2$ as byproduct whereas R4, R5 and R11 have free activation energies around 25 kcal·mol^{-1} and produce ${}^2N=(CH_3)_2$. Free activation energy difference between these two sets of reactions is roughly 5 kcal·mol^{-1} and it can be explained by the relative stability of their radical byproducts. In R3 and R9 a species with a terminal carbon centered radical forms, while the byproducts of R4, R5 and R11 contain a non-terminal nitrogen-centered radical. Higher radical stabilization through hyperconjugation is achieved by ${}^2N=(CH_3)_2$ rather than $(CH_3)_2NCH_2{}^2CH_2$ because the former radical species has one more alkyl group to perform hyperconjugation. Even though reactions R5 and R12 both yield ethylene, their free energy of activation difference is 9.4 kcal·mol^{-1}. They both contain a nitrogen centered radical as a product, however they differ in the resonance stability of these radical species. ${}^2N_3$ can delocalize the radical between three nitrogen atoms whereas ${}^2N=(CH_3)_2$ cannot resonate the radical. Reaction 10 exhibits the lowest free energy of activation (6.8 kcal·mol^{-1}) . This can be linked to the resonance stability of both of its products. $(CH_3)_2NCH=CH_2$ can have a resonance between the double bond and the lone pair of the nitrogen. Furthermore, the proximity of N_3 group to the free radical on carbon atom in TS10 and TS12 resulted in lower free energy barriers.

In R9 and R11, C-N_a bond breaks and C-N_a bond lengths of their corresponding reactants INT6 and INT8 are both 1.45 Å whereas in R10 and R12 C-N_b bond breaks and C-N_b bond lengths of their corresponding reactants INT7 and INT9 are 1.51 Å and 1.49 Å. Even though the C-N_a bond of INT6 and INT8 are shorter than the C-N_b bond of INT7 and INT9, C…N_a distance in TS9 and TS11 are longer than C…N_b distance in TS10 and TS12. As a result R10 and R12 have the lowest free energy barriers discussed in β scission reactions with values 6.8 kcal·mol^{-1} and 15.2 kcal·mol^{-1}.

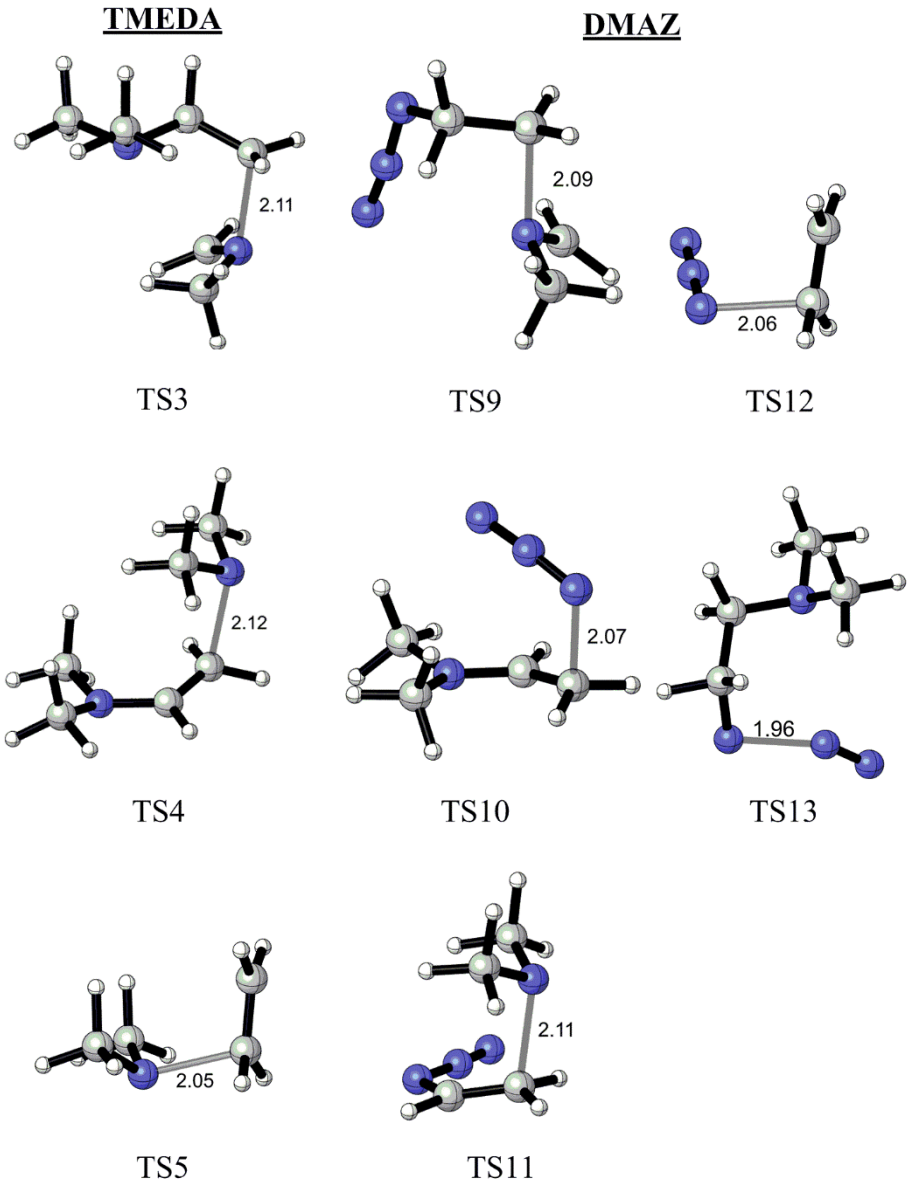

Figure 4.7. Transition state structures for bond fission reactions in TMEDA and DMAZ, bond distances are in Å (M06-2X/6-31++G(d,p)).

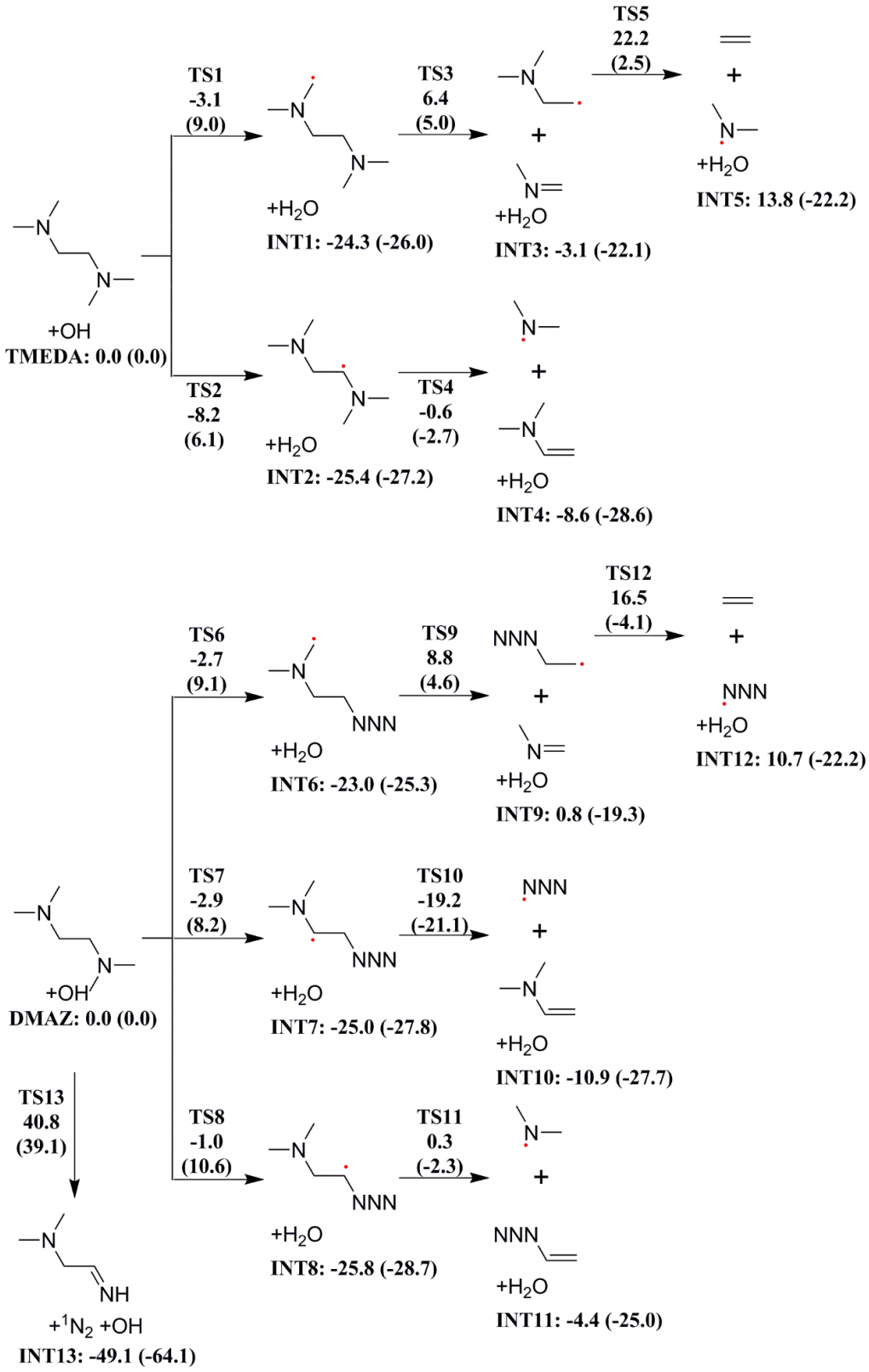

Figure 4.8. Ignition reactions of TMEDA and DMAZ.

Enthalpy and free energy (in parenthesis) at 423K and 1atm for TMEDA/NA and DMAZ/NA combustion.

If the free energy change achieved by the end of the reactions are examined, the values are -22.2, -28.6 kcal·mol^{-1} for TMEDA and -22.2, -25.0, -27.7 kcal·mol^{-1} for DMAZ (Scheme 3). Even though these results are very similar for TMEDA and DMAZ, free energy barriers for β Scission reactions are much lower for DMAZ.

4.3.2.3. N-N_2 Bond Fission

Bond fission reaction between N-N_2 in DMAZ is investigated to compare with H-abstraction and bond fission mechanisms shown in Figure 4.7. and Figure 4.8..

R13: $(CH_3)_2NCH_2CH_2NNN \rightarrow (CH_3)_2NCH_2CH{=}NH + N_2$

This bond fission reaction where $^1N_2$ forms, clearly has a much higher free energy barrier (39.1 kcal·mol^{-1}) however its free energy of reaction is also much lower (-64.1 kcal·mol^{-1}) than any other reaction considered before.

4.4. Conclusion

In this study, the hypergolic reactions of WFNA with TMEDA and DMAZ has been carried out with DFT. It is expected to shed light on the rationalization of the ignition delay time of the TMEDA/WFNA, DMAZ/WFNA and TMEDA(2) /DMAZ (1) /WFNA mixtures as well as on the synergistic of the TMEDA(2) /DMAZ (1) /WFNA mixture decreasing the ignition delay time when mixed in 2:1 proportion. Four major findings are of interest:

1) TMEDA supplies much more energy than DMAZ via salt formation exothermicity.
2) H-abstraction reactions have close free energetic results for TMEDA and DMAZ.
3) β scission reactions of DMAZ are faster than the ones for TMEDA because DMAZ has lower barrier heights due to the substitution of amine group with the azido group.
4) N-N_2 bond fission reaction of DMAZ has the highest energy barrier among the ignition reactions but it also has a much higher exothermicity than the other ignition reactions.

According to these results, TMEDA exhibiting a higher exothermicity for the salt formation reaction may be dominating factor in the lower ignition delay time of TMEDA because it can be seen that H-abstraction results are similar for TMEDA and DMAZ and β scission reactions favor faster ignition of DMAZ.

Considering the 2:1 TMEDA:DMAZ mixture, TMEDA is clearly responsible for heat generation through salt formation. Together with higher supplied energy, DMAZ can contribute through either faster β scission reactions or heat generation through the $N\text{-}N_2$ bond fission reaction. Reactions between DMAZ and HNO_3 may not be able to produce enough heat for the unimolecular $N\text{-}N_2$. Hence if this reaction occurs via the heat supplied by the TMEDA-dinitrate salt formation, it would result in more heat generation, rendering the ignition faster. Consequently, synergistic effect observed in 2:1 TMEDA:DMAZ mixture can be explained at the quantum mechanistic level.

In light of H-abstraction reactions, •OH facilitates these reactions rather than NO_2 for both TMEDA and DMAZ. These results are in agreement with the Reactive Molecular Dynamics (RMD) results of Needham.[35]

REFERENCES

1. T. Noda and Y. Shirota, “5,5’-Bis(dimesitylboryl)-2,2’-bithiophene and 5,5’-Bis(dimesitylboryl)- 2,2’:5’, 2’’-terthiophene as a novel family of electron-transporting amorphous molecular materials [18],” *J. Am. Chem. Soc.*, vol. 120, no. 37, pp. 9714–9715, 1998.
2. T. Noda, H. Ogawa, and Y. Shirota, “Blue-emitting organic electroluminescent device using a novel emitting amorphous molecular material, 5,5′-bis(dimesitylboryl)-2,2′-bithiophene,” *Adv. Mater.*, vol. 11, no. 4, pp. 283–285, 1999.
3. T. Noda and Y. Shirota, “Blue-emitting organic electroluminescent device using a novel emitting amorphous molecular material,” *J. Lumin.*, vol. 87, pp. 1168–1170, 2000.
4. C. D. Entwistle, J. C. Collings, A. Steffen, L. O. Pålsson, A. Beeby, D. Albesa-Jové, J. M. Burke, A. S. Batsanov, J. A. K. Howard, J. A. Mosely, S. Y. Poon, W. Y. Wong, F. Ibersiene, S. Fathallah, A. Boucekkine, J. F. Halet, and T. B. Marder, “Syntheses, structures, two-photon absorption cross-sections and computed second hyperpolarisabilities of quadrupolar A-π-A systems containing E-dimesitylborylethenyl acceptors,” *J. Mater. Chem.*, vol. 19, no. 40, pp. 7532–7544, 2009.
5. J. U. Lee, J. W. Jung, J. W. Jo, and W. H. Jo, “Degradation and stability of polymer-based solar cells,” *J. Mater. Chem.*, vol. 22, no. 46, pp. 24265–24283, 2012.
6. L. Carlsen, B. N. Kenessov, and S. Y. Batyrbekova, “A QSAR/QSTR study on the human health impact of the rocket fuel 1,1-dimethyl hydrazine and its transformation products. Multicriteria hazard ranking based on partial order methodologies,” *Environ. Toxicol. Pharmacol.*, 2009.
7. D. E. Bittner, J. L. Sell, and G. A. Risha, “Effect of Jet Momentum Ratio and Equivalence Ratio on the Ignition Process of TMEDA and White Fuming Nitric Acid (WFNA),” pp. 1–12, 2013.
8. A. R. Leach, “Molecular modelling : principles and applications Second Edition,” *Pearson Educ. EMA*, p. 784, 2001.
9. C. J. Cramer, *Essentials of Computational Chemistry: Theories and Models*. 2004.
10. R. Peverati and D. G. Truhlar, “Quest for a universal density functional: The accuracy

of density functionals across a broad spectrum of databases in chemistry and physics," *Philosophical Transactions of the Royal Society A: Mathematical, Physical and Engineering Sciences*, vol. 372, no. 2011. 2014.

11. S. F. Sousa, P. A. Fernandes, and M. J. Ramos, "General performance of density functionals," *J. Phys. Chem. A*, vol. 111, no. 42, pp. 10439–10452, 2007.
12. N. Engineering, "Evaluation of B3LYP , X3LYP , and M06-Class Density Functionals for Predicting the Binding Energies of Neutral , Protonated , and Deprotonated Water Clusters," *J. Chem. Theory Comput.*, pp. 1–14, 2008.
13. Y. Zhao, D. G. Truhlar, Y. Zhao, and D. G. Truhlar, "The M06 suite of density functionals for main group thermochemistry, thermochemical kinetics, noncovalent interactions, excited states, and transition elements: two new functionals and systematic testing of four M06-class functionals and 12 other function," *Theor Chem Acc.*, vol. 120, pp. 215–241, 2008.
14. T. Helgaker, P. Jørgensen, and J. Olsen, "Gaussian Basis Sets," in *Molecular Electronic-Structure Theory*, 2000.
15. J. Tomasi, B. Mennucci, and R. Cammi, "Quantum mechanical continuum solvation models," *Chemical Reviews*, vol. 105, no. 8. pp. 2999–3093, 2005.

16 C. J. Cramer and D. G. Truhlar, "Implicit Solvation Models: Equilibria, Structure, Spectra, and Dynamics," *Chem. Rev.*, vol. 99, no. 8, pp. 2161–2200, 1999.

17. B. Vincenzo, C. Maurizio, and T. Jacopo, "Geometry optimization of molecular structures in solution by the polarizable continuum model," *J. Comput. Chem.*, vol. 19, no. 4, pp. 404–417, 1998.
18. V. Barone and M. Cossi, "Quantum calculation of molecular energies and energy gradients in solution by a conductor solvent model," *J. Phys. Chem. A*, vol. 102, no. 11, pp. 1995–2001, 1998.
19. B. Mennucci, E. Cancès, and J. Tomasi, "Evaluation of Solvent Effects in Isotropic and Anisotropic Dielectrics and in Ionic Solutions with a Unified Integral Equation Method: Theoretical Bases, Computational Implementation, and Numerical Applications," *J. Phys. Chem. B*, vol. 101, no. 49, pp. 10506–10517, 1997.
20. B. Mennucci and J. Tomasi, "Continuum solvation models: A new approach to the problem of solute's charge distribution and cavity boundaries," *J. Chem. Phys.*, vol. 106, no. 12, pp. 5151–5158, 1997.

21 M. Marazzi, T. Schnappinger, L. González, A. Monari, R. de Vivie-Riedle, and P.

Kölle, “Ab initio molecular dynamics of thiophene: the interplay of internal conversion and intersystem crossing,” *Phys. Chem. Chem. Phys.*, vol. 19, no. 37, pp. 25662–25670, 2017.

22. S. Mai, A. Monari, M. Marazzi, T. Schnappinger, R. de Vivie-Riedle, and L. González, “Intersystem Crossing as a Key Component of the Nonadiabatic Relaxation Dynamics of Bithiophene and Terthiophene,” *J. Chem. Theory Comput.*, vol. 14, no. 9, pp. 4530–4540, 2018.
23. O. Sengul, M. Marazzi, A. Monari, and S. Catak, “Photophysical Properties of Novel Two-Photon Absorbing Dyes: Assessing Their Possible Use for Singlet Oxygen Generation,” *J. Phys. Chem. C*, vol. 122, no. 28, pp. 16315–16324, 2018.
24. A. Facchetti, “Semiconductors for organic transistors,” *Mater. Today*, vol. 10, no. 3, pp. 28–37, 2007.
25. J. Zaumseil and H. Sirringhaus, “Electron and ambipolar transport in organic field-effect transistors,” *Chem. Rev.*, vol. 107, no. 4, pp. 1296–1323, 2007.
26. S. R. Forrest and M. E. Thompson, “Introduction: Organic electronics and optoelectronics,” *Chem. Rev.*, vol. 107, no. 4, pp. 923–925, 2007.
27. S. Reineke, F. Lindner, G. Schwartz, N. Seidler, K. Walzer, B. Lüssem, and K. Leo, “White organic light-emitting diodes with fluorescent tube efficiency,” *Nature*, vol. 459, no. 7244, pp. 234–238, 2009.
28. Y.-J. Cheng, S.-H. Yang, and C.-S. Hsu, “Synthesis of Conjugated Polymers for Organic Solar Cell Applications,” pp. 5868–5923, 2009.
29. M. Grätzel, “Dye-sensitized solar cells,” *J. Photochem. Photobiol. C …*, vol. 4, no. 2, pp. 145–153, 2003.
30. H. T. Turan, O. Kucur, B. Kahraman, S. Salman, and V. Aviyente, “Design of donor-acceptor copolymers for organic photovoltaic materials: A computational study,” *Phys. Chem. Chem. Phys.*, vol. 20, no. 5, pp. 3581–3591, 2018.
31. C. Hoffend, M. Diefenbach, E. Januszewski, M. Bolte, H. W. Lerner, M. C. Holthausen, and M. Wagner, “Effects of boron doping on the structural and optoelectronic properties of 9,10-diarylanthracenes,” *Dalt. Trans.*, vol. 42, no. 38, pp. 13826–13837, 2013.
32. H. T. Turan, Y. Eken, M. Marazzi, M. Pastore, V. Aviyente, and A. Monari, “Assessing One- and Two-Photon Optical Properties of Boron Containing Arenes,” *J. Phys. Chem. C*, vol. 120, no. 32, pp. 17916–17926, 2016.

33. W. R. Mateker and M. D. McGehee, “Progress in Understanding Degradation Mechanisms and Improving Stability in Organic Photovoltaics,” *Adv. Mater.*, vol. 29, no. 10, 2017.
34. J. H. Lee and I. N. Tang, “Absolute rate constants for the hydroxyl radical reactions with ethane, furan, and thiophene at room temperature,” *J. Chem. Phys.*, vol. 77, no. 9, pp. 4459–4463, 1982.
35. R. Atkinson, S. M. Aschmann, and W. P. L. Carter, “Kinetics of the reactions of O3and OH radicals with furan and thiophene at 298 ± 2 K,” *Int. J. Chem. Kinet.*, vol. 15, no. 1, pp. 51–61, 1983.
36. Y. Zhang, J. Sun, Y. Sun, Y. Tang, and R. Wang, “Mechanistic and kinetic study on the reaction of thiophene with hydroxyl radical,” *Comput. Theor. Chem.*, vol. 1092, pp. 74–81, 2016.
37. R. Atkinson, S. M. Aschmann, and J. N. Pitts, Jr., “Rate constants for the gas-phase reactions of the NO3 radical with a series of organic compounds at 296 ± 2 K,” *J. Phys. Chem.*, vol. 92, no. 34, pp. 3454–3457, 1988.
38. B. Cabañas, M. T. Baeza, P. Martín, S. Salgado, F. Villanueva, E. Monedero, and K. Wirtz, “Products and mechanism of the NO3 reaction with thiophene,” *J. Atmos. Chem.*, vol. 51, no. 3, pp. 317–335, 2005.
39. W. Zhang, T. Wang, C. Feng, B. Du, and L. Mu, “Computational studies on the mechanisms for the gas-phase reaction between thiophene and NO3,” *Chem. Phys. Lett.*, vol. 467, no. 1–3, pp. 52–57, 2008.
40. X. Song, M. G. Fanelli, J. M. Cook, F. Bai, and C. A. Parish, “Mechanisms for the reaction of thiophene and methylthiophene with singlet and triplet molecular oxygen,” *J. Phys. Chem. A*, vol. 116, no. 20, pp. 4934–4946, 2012.
41. M. Manceau, A. Rivaton, and J. L. Gardette, “Involvement of singlet oxygen in the solid-state photochemistry of P3HT,” *Macromol. Rapid Commun.*, vol. 29, no. 22, pp. 1823–1827, 2008.
42. M. Manceau, J. Gaume, A. Rivaton, J. L. Gardette, G. Monier, and L. Bideux, “Further insights into the photodegradation of poly(3-hexylthiophene) by means of X-ray photoelectron spectroscopy,” *Thin Solid Films*, vol. 518, no. 23, pp. 7113–7118, 2010.
43. H. Ohta and H. Koizumi, “Mechanisms of photo-induced degradation of polythiophene derivatives: re-examination of the role of singlet oxygen,” *Polym.*

Bull., vol. 74, no. 6, pp. 2319–2330, 2017.

44 A. Becke, "B3LYP," *J. Chem. Phys.*, 1993.

45. N. Sai, K. Leung, J. Zádor, and G. Henkelman, "First principles study of photo-oxidation degradation mechanisms in P3HT for organic solar cells," *Phys. Chem. Chem. Phys.*, vol. 16, no. 17, pp. 8092–8099, 2014.

46. T. Saito, S. Nishihara, Y. Kataoka, Y. Nakanishi, Y. Kitagawa, T. Kawakami, S. Yamanaka, M. Okumura, and K. Yamaguchi, "Projection Method . Comparison with Multireference Coupled-Cluster Calculations," *J. Phys. Chem. A*, vol. 114, pp. 7967–7974, 2010.

47. J. Méndez-Hurtado, R. Lõpez, D. Suárez, and M. I. Menéndez, "Theoretical study of the oxidation of histidine by singlet oxygen," *Chem. - A Eur. J.*, vol. 18, no. 27, pp. 8437–8447, 2012.

48. J. A. Kerr, R. C. Sekhar, and A. F. Trotman-Dickenson, "599. The pyrolyses of hydrazines and benzylamines. C–C and N–N bond dissociation energies," *J. Chem. Soc.*, 2004.

49. I. J. Eberstein and I. Glassman, "The gas-phase decomposition of hydrazine and its methyl derivatives," in *Symposium (International) on Combustion*, 1965.

50. D. M. Golden, R. K. Solly, N. A. Gac, and S. W. Benson, "Very low-pressure pyrolysis. VII. The decomposition of methylhydrazine, 1,1-dimethylhydrazine, 1,2-dimethylhydrazine, and tetramethylhydrazine. Concerted deamination and dehydrogenation of methylhydrazine," *Int. J. Chem. Kinet.*, 1972.

51. I. Stevenson William H., L. D. Felton, and Z. Slocum-Wang, "Hypergolic liquid or gel rocket fuel mixtures for use in bipropellant propulsion systems.," 2008.

52. S. Wang, S. T. Thynell, and A. Chowdhury, "Experimental study on hypergolic interaction between N,N,N′,N′ -tetramethylethylenediamine and nitric acid," *Energy and Fuels*, vol. 24, no. 10, pp. 5320–5330, 2010.

53. W. G. Liu, S. Dasgupta, S. V. Zybin, and W. A. Goddard, "First principles study of the ignition mechanism for hypergolic bipropellants: N,N,N',N'-tetramethylethylenediamine (TMEDA) and N,N,N',N'-tetramethylmethylenediamine (TMMDA) with nitric acid," *J. Phys. Chem. A*, vol. 115, no. 20, pp. 5221–5229, 2011.

54. P. Zhang, L. Zhang, and C. K. Law, "Density functional theory study of the reactions of 2-azido-N,N-dimethylethanamine with nitric acid and nitrogen dioxide," *Combust.*

Flame, vol. 162, no. 1, pp. 237–248, 2015.

55. N. J. Labbe, "Determining Detailed Reaction Kinetics for Nitrogen- and Oxygen-Containing Fuels," 2013.
56. C. D. Needham, "Crafting Detailed Kinetic Mechanisms for Gas- and Condensed-Phase Systems using Computational Quantum Chemistry" 2016.
57. C. C. Chen and M. J. McQuaid, "Mechanisms and kinetics for the thermal decomposition of 2-azido- N, N -dimethylethanamine (DMAZ)," *J. Phys. Chem. A*, vol. 116, no. 14, pp. 3561–3576, 2012.
58. G. M. J. Frisch, W. Trucks, H. B. . Schlegel, *et al.*, *Gaussian 09, Revision E. 01; Gaussian*. 2009.
59. J. P. Cerón-Carrasco and D. Jacquemin, "Interplay between hydroxyl radical attack and H-bond stability in guanine-cytosine," *RSC Adv.*, vol. 2, no. 31, pp. 11867–11875, 2012.
60. B. K. Mishra, M. Lily, A. K. Chakrabartty, D. Bhattacharjee, R. C. Deka, and A. K. Chandra, "Theoretical investigation of atmospheric chemistry of volatile anaesthetic sevoflurane: Reactions with the OH radicals and atmospheric fate of the alkoxy radical (CF3)2CHOCHFO: Thermal decomposition vs. oxidation," *New J. Chem.*, vol. 38, no. 7, pp. 2813–2822, 2014.
61. N. Dmaz, C. Chen, and M. Mcquaid, "A Thermochemical Kinetic-Based Study of Ignition Delays for 2-Azidoethanamine-Red Fuming Nitric Acid Systems :," no. January, 2014.
62 P. Zhang, L. Zhang, and C. K. Law, "Density functional theory study of the reactions of 2-azido-N,N-dimethylethanamine with nitric acid and nitrogen dioxide," *Combust. Flame*, vol. 162, no. 1, pp. 237–248, 2015.
63. N. J. Labbe, "Determining Detailed Reaction Kinetics for Nitrogen- and Oxygen-Containing Fuels," 2013.
64. G. S. Hammond, "A Correlation of Reaction Rates," *J. Am. Chem. Soc.*, 1955.